LBL-38437
UC-404

Center for Advanced Materials

CAM

Solid Phase Epitaxial Regrowth of (100)GaAs

M.I. Almonte
(M.S. Thesis)

February 1996

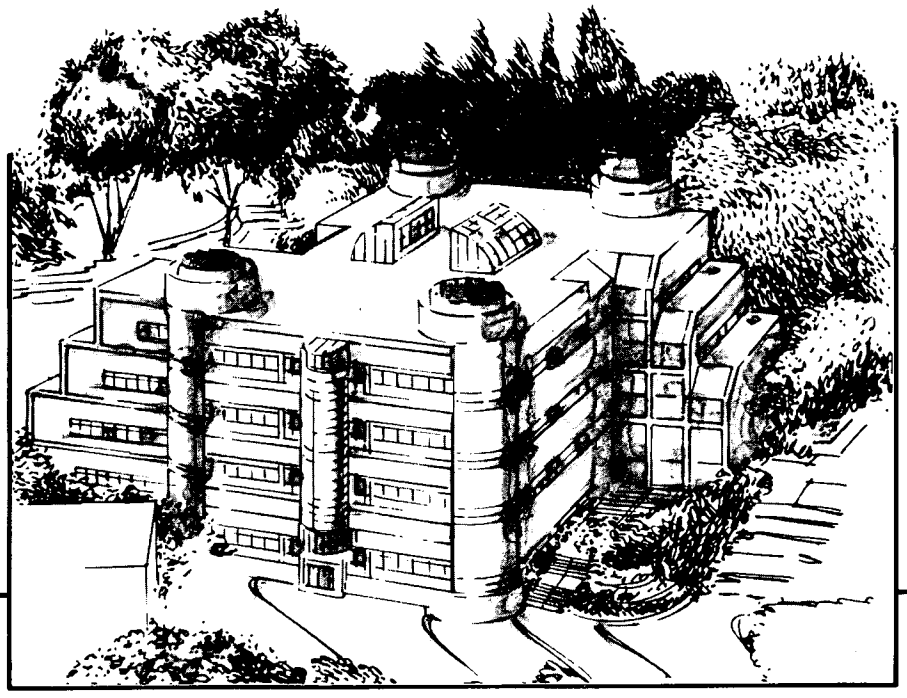

Materials and Chemical Sciences Division
Lawrence Berkeley Laboratory • University of California
ONE CYCLOTRON ROAD, BERKELEY, CA 94720 • (415) 486-4755

Prepared for the U.S. Department of Energy under Contract DE-AC03-76SF00098

REFERENCE COPY
Does Not
Circulate
Bldg. 50 Library.
LBL-38437
Copy 1

DISCLAIMER

This document was prepared as an account of work sponsored by the United States Government. While this document is believed to contain correct information, neither the United States Government nor any agency thereof, nor the Regents of the University of California, nor any of their employees, makes any warranty, express or implied, or assumes any legal responsibility for the accuracy, completeness, or usefulness of any information, apparatus, product, or process disclosed, or represents that its use would not infringe privately owned rights. Reference herein to any specific commercial product, process, or service by its trade name, trademark, manufacturer, or otherwise, does not necessarily constitute or imply its endorsement, recommendation, or favoring by the United States Government or any agency thereof, or the Regents of the University of California. The views and opinions of authors expressed herein do not necessarily state or reflect those of the United States Government or any agency thereof or the Regents of the University of California.

LBL-38437

Solid Phase Epitaxial Regrowth of (100)GaAs

Marlene Isabel Almonte
M.S. Thesis

Materials Science and Mineral Engineering
University of California, Berkeley

and

Materials Sciences Department
Ernest Orlando Lawrence Berkeley National Laboratory
University of California
Berkeley, CA 94720

February 1996

This work was supported by the Director, Office of Energy Research, Office of Basic Energy Sciences, Materials Sciences Division, of the U.S. Department of Energy under Contract No. DE-AC03-76SF00098.

Solid Phase Epitaxial Regrowth of (100)GaAs

by

Marlene Isabel Almonte

B. S. (Rensselaer Polytechnic Institute) 1992

A thesis submitted in partial satisfaction of the

requirements for the degree of

Master of Science

in

Engineering-Materials Science and Mineral Engineering

in the

GRADUATE DIVISION

of the

UNIVERSITY of CALIFORNIA at BERKELEY

Committee in charge:

Professor Eugene E. Haller, Chair
Dr. Kin Man Yu
Professor Timothy Sands

1996

Table of Contents

1. Introduction 1

1.1 Some Properties of and Processes in Semiconductor Materials 4

1.1.1 Band Structures of Si, Ge, and GaAs 4

1.1.2 Electronic Transport 7

1.1.3 Optical Generation and Recombination of Carriers 11

1.2 GaAs Device Basics 14

1.3 Solid Phase Epitaxy and Motivation of This Research 18

1.4 Previous Studies of Solid Phase Epitaxy in GaAs 23

2. Radiation Damage 25

2.1 Ion Implantation 25

2.2 Defects in Semiconductors 29

2.3 Radiation Damage in Semiconductors 30

2.4 Ion Implantation Damage and Amorphization of GaAs 35

2.5 Transport of Ions in Matter (TRIM) 39

3. Fundamentals of Solid Phase Epitaxy 43

3.1 Regrowth Kinetics in Si 43

3.2 Regrowth Kinetics in GaAs 46

4. Influence of Implantation Parameters on Damage Distribution 50

5. Characterization Techniques 56

5.1 Rutherford Backscattering Spectrometry (non-channeled and channeled) 56

5.1.1 Basic Principles of Rutherford Backscattering Spectrometry (RBS) 56

5.1.2 Ion Channeling 63

5.2 Raman Spectroscopy 67

5.3 Transmission Electron Microscopy 73

6. Experimental Conditions 74

6.1 Sample Preparation 74

6.1.1 Implant Conditions 74

6.1.2 Isochronal and Isothermal Annealing 76

6.2 Characterization 76

6.2.1 Rutherford Backscattering Spectrometry 76

6.2.2 Raman Spectroscopy 76

6.2.3 Transmission Electron Microscopy 76

7. Results and Discussion 78

8. Conclusions 104

9. References 106

Appendix:

Appendix I: Implant Conditions 110

Acknowledgments

I would like to thank Professor Eugene Haller for suggesting this masters project, and I am very grateful for his continual guidance and support. Furthermore, I wish to thank him for teaching me many essentials of technical writing as he patiently read through revised versions of this thesis. Dr. Kin Man Yu provided continued assistance with Rutherford Backscattering Spectrometry. I am very grateful for his expertise in solid phase regrowth of GaAs and for his help with data interpretation. I wish to thank Dr. Kin Man Yu and Professor Timothy Sands for reviewing this thesis. I would like to extend my gratitude to Dr. Amy Moll for teaching me some fundamentals of ion implanted GaAs.. Wlaldek Walukiewicz helped me with many discussions on solid phase epitaxy of GaAs. Kevin Roderick performed all of the implantations used for my research. Dr. Zuzanna Liliental-Weber and Jacek Jasinski performed the TEM work on my samples, which complemented the other characterization techniques. I am grateful to Dr. Joel Ager III, Dr. Lei Wang, and Dr. Anthony Chen for their assistance with Raman Spectroscopy.

I would like to say "*gracias*" to my fellow graduate students and friends in the Haller group. It was through their interaction, guidance, and endless support that I have learned the essentials for succeeding in graduate school.

I am grateful to the University of California (Graduate Opportunity Program Award) and the American Association of University Women (Selected Professions Fellowship) for their financial support. This work was supported by the Director, Office of Energy Research, Office of Basic Energy Sciences, Materials Science Division of the U.S. Department of Energy under Contract No. DE-AC03-76SF00098.

"Her presence influenced who I was, and her absence influences who I am" (wrote Hope Edelman in Motherless Daughters). I am eternally grateful to my mom, Hilda Almonte, for her encouragement and everlasting inspiration. To her I dedicate this thesis.

As focused as I am in school, my life would be empty without my family and close friends. I wish to thank my dad and my "sisters", Ana, Michelle, and Silvia for providing me with the motivation, courage, and strength to persevere in difficult times. They are the "wind beneath my wings". I am indebted to the Olivos for their numerous encouraging letters, Hallmark cards, and phone calls expressing their love and support. I would like to extend "*gracias*" to all my friends for their encouragement. Each one of them will always have a special place in my heart.

To my friend of ten years and future husband, Victor Olivo, who has walked with me hand in hand through many difficult times "*gracias*". Thanks for understanding my commitment to education and for being supportive in my endeavors.

1. Introduction

The worldwide prevalence of computers and other information processing and distribution equipment can be attributed to the availability of semiconductor devices, especially integrated circuits contained on small single crystal chips of Si (integration of individual resistors, capacitors, and transistors). Si is unquestionably the most widely used member of a group of materials called semiconductors. As suggested by their name, semiconductors are neither good electrical conductors (e.g. metals) nor good electrical insulators. Instead their ability to conduct electricity is intermediate and strongly depends on doping i.e., the presence of specific impurity atoms. Electrical resistivity values at room temperature for semiconductors range from 10^{-2} to 10^{9} Ω-cm. In contrast to metals the electrical resistivity of undoped semiconductors strongly depends on temperature. Si and Ge are elemental semiconductors, whereas GaAs and InP belong to a very large family of compound semiconductors.

An intrinsic semiconductor is essentially "free of impurities". Conduction results from the thermal promotion of electrons from a filled valence band in which they are immobile to an empty conduction band in which they can move. The removal of electrons, the negative charge carriers, from the valence band produces holes which act like mobile positive charge carriers. This intrinsic conduction at room temperature is possible because of the relatively small energy band gap between the valence and conduction band in semiconductors. Semiconductors have a band gap of the order of 0.5 to 3 eV.

Extrinsic semiconductors are materials to which impurities have been intentionally added. These impurity additions are called dopants, and the process of adding these components is known as doping. Dopant atoms produce energy levels within the band gap. The energy of shallow dopants lie close to the band edges and are easily ionized at room temperature. Each ionized dopant atom can contribute a free charge carrier.

A dopant in a semiconductor acts either as a donor or an acceptor when it occupies a substitutional lattice site, depending on whether it has an extra or missing valence electron, respectively. For instance, for GaAs if a column VI element (e.g., Se or Te) substitutes an As site, it is a donor. Likewise, if a column II element (e.g., Zn) sits on a Ga site, the dopant is an acceptor. Si can act as a donor on a Ga site or as an acceptor on an As site. Due to this dual role, Si is known as an amphoteric dopant. In theory, any group IV element in GaAs is amphoteric. However, it has been observed that certain group IV elements prefer one particular lattice site. For example, C in GaAs always acts as an acceptor or remains neutral (i.e., it assumes an As site or it is electrically inactive in precipitates) (Moll et al. 1993).

Diffusion is a technique which is widely used for the incorporation of dopant atoms into a semiconductor. The diffusion of impurities in semiconductors (e.g. Si) has been studied in great detail since the performance of devices depends critically on the impurity concentration and the impurity profile.

While diffusion can be performed with relatively inexpensive equipment it has some important shortcomings. First, very high temperature and long times are required. This can lead to severe contamination which has to be controlled with sophisticated

gettering schemes. Second, diffusion profiles are simple in nature (they can be typically described with complementary error or Gaussian functions). For complex dopant concentration profiles other techniques must be utilized.

For applications where a high reproducibility and sophisticated dopant concentration profiles are required, ion implantation technology offers many choices. In ion implantation, a beam of dopant ions of fixed energy (typically keV) is rastered across the surface of the semiconductor. The penetration depth of these ions is determined by the mass and energy of these ions as well as the mass of the target atoms. Implants of ions with different energies can be superimposed to yield complex dopant concentration profiles. One of the disadvantages of this method of doping is that the energetic ions displace target atoms, resulting in damage to the crystal structure (radiation damage). Subsequently, high temperature processing is required to anneal the disorder. Thermally annealing has to be carefully controlled since high temperatures can lead to diffusion of dopants and redistribution of dopant profiles. However, temperatures are lower and times are shorter for ion implantation doping than diffusion doping.

Solid Phase Epitaxy (SPE) is a crystal growth process which can be used to remove lattice damage and activate implanted dopants, while minimizing the amount of dopant diffusion. SPE proceeds at relatively low temperatures and it is widely used for the electrical activation of dopants in extremely thin ion implanted layers and for sharp interfacial doping profiles. The epitaxial regrowth behavior of an implanted layer plays an important role in the electrical properties of that layer.

Extensive work has been performed on the SPE of Si using self-ion implantation (Si amorphized by Si implantation). A pure amorphous layer can be created for the study of intrinsic SPE regrowth processes with this self-ion implantation technique. SPE regrowth process is of considerable interest for GaAs devices which requires ion implantation doping.

It has been observed that the reordering of amorphous ion implanted GaAs (Sadana et al. 1984 and Gamo et al. 1977) is not as simple an epitaxial process as observed in Si. Very few studies of pure amorphous layers formed by ion implantation (e.g. Ga and As implantation) in GaAs have been reported. In this work, I report on detailed studies of solid phase epitaxial processes of stoichiometrically balanced ion implanted GaAs layers.

1.1 Some Properties of and Processes in Semiconductor Materials

The performance of semiconductor devices is affected by a variety of physical properties. The properties which are crucial for opto-electronic applications will be reviewed and high speed digital integrated circuits will be emphasized.

1.1.1 Band Structures of Si, Ge, and GaAs

Si and Ge are covalently bonded materials while GaAs is mainly covalent with some ionicity. Covalent bonding involves sharing of valence electrons between atoms. The shared electrons orbit around both atoms. The overlap of bonding orbitals lowers the energy of the system. Since the valence electrons form covalent bonds, no free electrons are available for charge transport.

In the energy band model, the valence band is associated with the covalently bound electrons and the conduction band with the free electrons. The energy gap between these bands corresponds to the energy required to break covalent bonds. Energy band diagrams illustrate the relation between energy (E) and wave vector (k). The energy band structures of Ge, Si, and GaAs are shown in figure 1.1. The bands above the gap are the conduction bands and the bands below the gap are the valence bands. The minimum band gap for each of the semiconductors is labeled by E_g. The band gap is the energy difference between the conduction band minimum and the valence band maximum. If light is shone on the semiconductor with photon energy greater than the band gap energy (1.1 eV for Si) the covalent bond can be broken. Subsequently, the electron is free to move within the crystal. Direct and indirect gap semiconductors will be discussed in section 1.13.

Another parameter which can be derived from the band structure is the effective mass. An electron in a solid travels with an effective mass which is different from the mass of a free electron. The effective mass of the carrier is inversely proportional to the curvature of the band, $(\partial^2E/\partial k^2)^{-1}$. The band structures in figure 1.1 show that the curvatures of the upper two valence bands are different. These are denoted as the heavy hole (smaller curvature) and light hole (larger curvature) bands. In Si the conduction band has six symmetry related minima points in the <100> directions in the Bruillouin zone. The constant energy surfaces near the conduction band minima are six ellipsoids with the long axes oriented along the <100> axes. The effective mass of the electron has a longitudinal effective mass (along the axes) of $0.92m_o$, and a transverse effective mass (perpendicular to axes) of $0.19m_o$ (see for example Kittel 1986) where m_o is the mass of

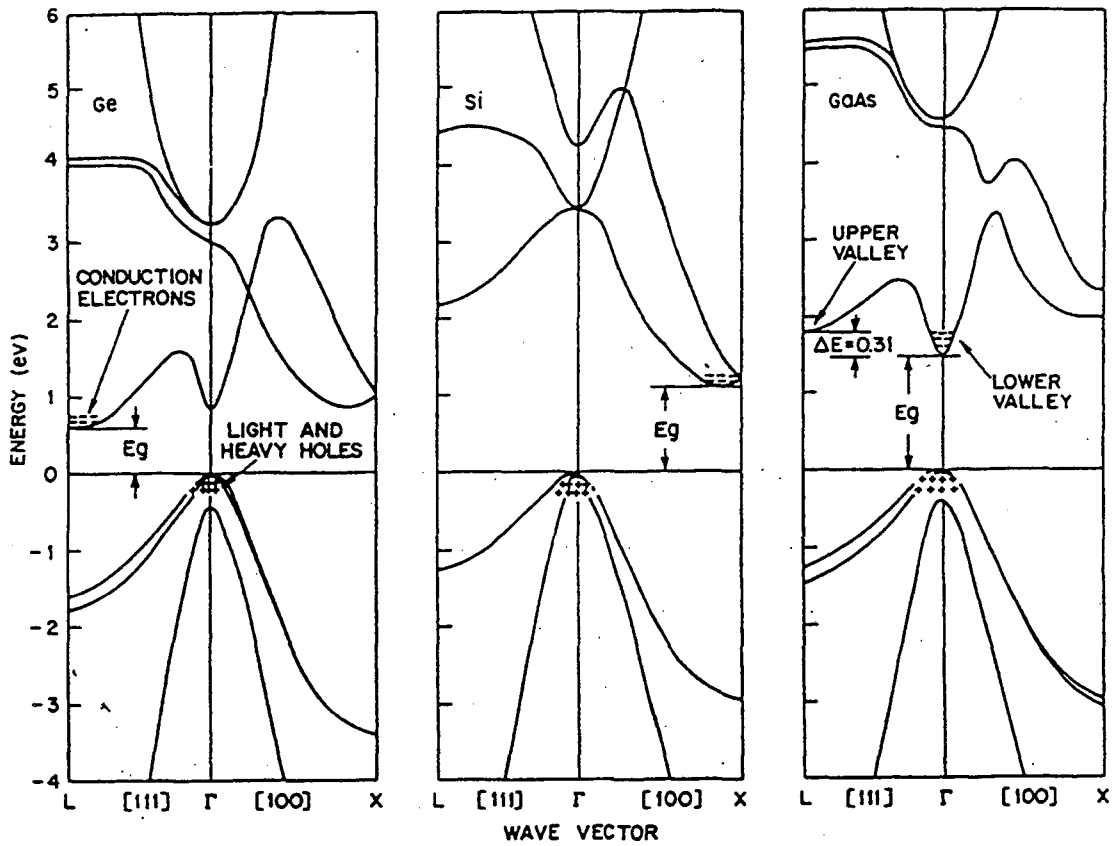

Figure 1.1 Energy band structures of Ge, Si, and GaAs. Plus (+) signs indicate holes in the valence bands and minus (-) signs indicate electrons in the conduction bands (Sze 1981).

the free electron. The conduction band minima in Ge occur at the zone boundaries in the <111> directions. There are four symmetry related conduction band minima. The constant energy surfaces are ellipsoids along the <111> directions. The longitudinal and transverse effective masses of the electrons are $1.59m_o$ and $0.082m_o$, respectively.

A few of the important properties of Si and GaAs at room temperature are presented in table 1.1.

1.1.2 Electronic Transport

In semiconductors, both negative (electrons) and positive (holes) charge carriers can contribute to current flow. In materials doped predominantly with donors electrons are the majority carriers. Similarly, holes are the majority charge carriers in p-type (doped with acceptors) semiconductors.

Under the influence of an applied field, an electron is accelerated along the field direction. The net carrier velocity in the applied field is called the drift velocity. The electron drift velocity at low fields (E) is given by eq. (1) (see for example Muller and Kamins 1986).

$$v_d = -\frac{q\tau}{m_n^*}E = -\mu E \qquad (1)$$

where m_n^* is the effective mass of the electron and τ is the mean scattering time. The effective mass may be substantially different than the free electron mass. As already mentioned in the previous chapter, this is a consequence of the band structure of the semiconductor and the quantum mechanical nature of electron transport. From eq.(1) we see that the electron drift velocity is proportional to the electric field. The proportionality

	Si	GaAs
electron mobility (cm^2/Vs)	**1417**	**8800**
hole mobility (cm^2/Vs)	**471**	**400**
electron effective mass (m_o=free electron mass)	**$1.08m_o$**	**$0.068m_o$**
hole effective mass	**$0.81m_o$**	**$0.50m_o$**
bandgap (eV)	**1.124**	**1.42**
crystal structure	**diamond cubic**	**zinc blende**

Table 1.1 Properties of Si and GaAs at room temperature (see for example K.Böer 1992).

factor is called the mobility μ. The mobility is a parameter which reflects all the interactions between the carrier and the crystal. The magnitude of the mobility is determined by the nature of the scattering events which the free carriers experiences in the semiconductor. Free carriers in a lattice can be scattered by lattice phonons, ionized impurities, neutral impurities, and crystal defects. Eq. (1) is valid only for low electric fields. In this regime, the drift velocity imparted to the free carrier by the applied field is much less than the random thermal velocity. At room temperature the random thermal velocity is about 10^7cm/s.

Electric fields are high when the drift velocity becomes comparable to the random thermal velocity. At this point the energy of the carrier no longer increases significantly as the applied electric field is increased. Carriers known as "hot carriers" lose energy through new processes. The most important one is the emission of optical phonons, the most energetic lattice vibrations. Figures 1.2 shows the variation in drift velocity with electric fields for Si (figure 1.2(a)) and GaAs (figure 1.2(b)). The electric field independent drift velocity is called the saturation velocity.

The current density flowing in the direction of an applied electric field for a semiconductor with electrons as charge carriers is given in eq. (2).

$$J = (nq\mu_e)E \tag{2}$$

Where q is the charge of the carrier, n is the carrier concentration, and μ_e is the electron mobility. The terms in the parentheses is the conductivity σ. Eq. (2) is also valid for positive charge carriers.

(a)

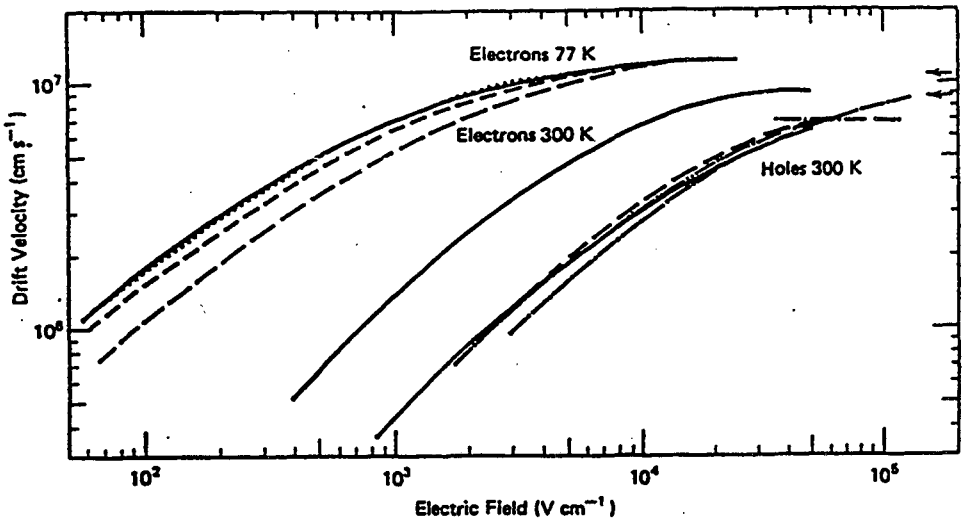

(b)

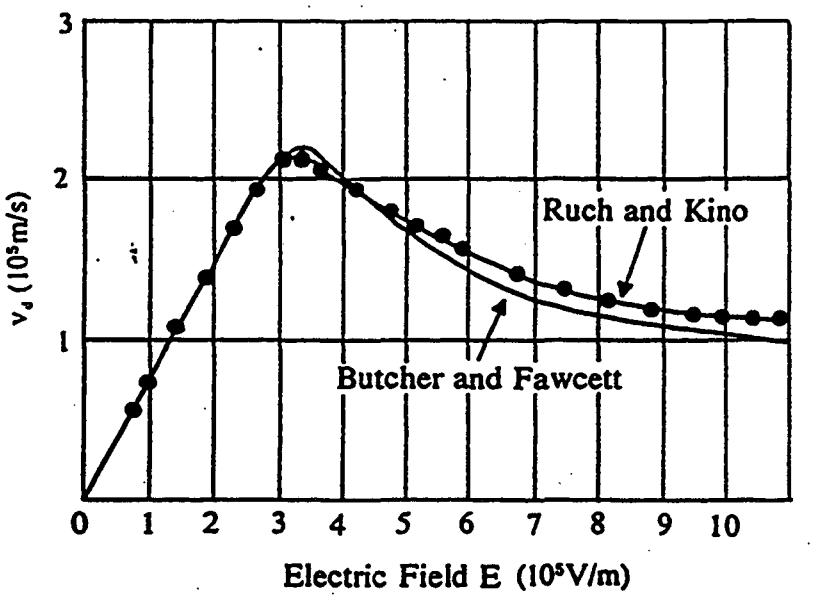

Figure 1.2 Drift velocity as a function of the electric field for (a) electrons and holes in Si (Muller 1986) (b) electrons in GaAs (Blackmore 1985). The bandstructure of GaAs leads to the mobility maximum at the relatively low field of ~3.5kV/cm.

1.1.3 Optical Generation and Recombination of Carriers

Photogeneration is a process whereby electrons and holes are created. In photogeneration photons with an energy greater than E_g impinge on the semiconductor and create electrons and holes by exciting electrons from the valence band into the conduction band. In terms of the bond model, this mechanism can be visualized as breaking bonds in the lattice and subsequently freeing electrons.

In recombination processes electrons and holes are mutually annihilated. Two kinds of recombination processes exists, radiative and non-radiative. In a radiative recombination event a photon is emitted with a frequency of $\nu=E_{gap}/h$ while in a non-radiative event phonons are created. The radiative efficiency of a semiconductor material, i.e., the ratio of radiative recombination events and total events, depends strongly on band structure and defects in the semiconductor.

We now briefly discuss the various kinds of recombination processes in semiconductor materials (figure 1.3). Figure 1.3(a) shows band-to-band recombination. In such a recombination event the energy released is equal to the band gap $E_{gap}=h\nu$. At this point, it is instructive to define the meaning of a direct band gap semiconductor material versus an indirect band gap. In a semiconductor with a direct band gap, the transition of an electron from the minimum of the conduction band to the top of the valence band occurs with no change in wave vector (momentum) (figure 1.3(a1)). In the indirect band gap material these band extrema are located at different positions in momentum space (Brillouin zone) and one or more phonons are required for recombination (figure 1.3(a2)). For the recombination event in figure 1.3(a2), an indirect

semiconductor requires a phonon for the conservation of momentum. Consequently in an indirect band gap material, this recombination event is a three particle process. This three particle process is much less likely to occur than the two particle process in a direct band gap semiconductor (GaAs). As a result, band-to-band recombination is less efficient in indirect band gap than in direct band gap materials. In addition to band-to-band radiative recombination one can observe photons generated in band-to-shallow state transitions as shown in figure 1.3(b). The energy of the photon emitted in such event is well defined and leads to sharp photo-luminescent lines. Their energy depends on the position of the shallow state within the band gap ($h\nu=E_{gap}-E_{shallow}$.).

Recombination to a state deep in the band gap is illustrated in figure 1.3(c). Because deep states are spread out in k-space the recombination can occur between a range of band states and the deep level leading to broad photoluminescence lines.

Auger recombination is a non-radiative transition (figure 1.3(d)). In this event, the energy released by the recombination of the electron and hole pair does not lead to the emission of a photon. The energy is transferred to another carrier which is excited high into its band and returns to the band minimum through the emission of many phonons. A recombination process exhibiting multiphonon transitions is illustrated in figure 1.3(e). In this multiphonon transition, the electron reaches the valence band and several phonons are emitted.

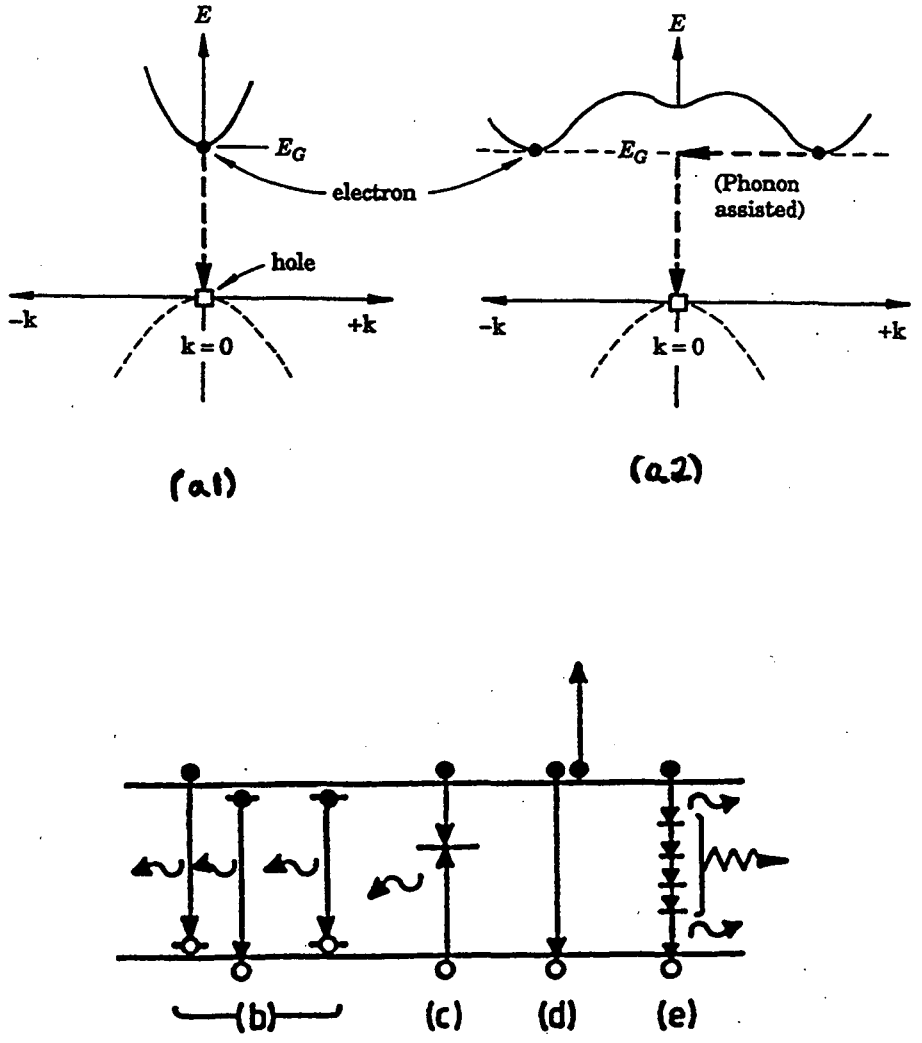

Figure 1.3 E-k diagrams of electron transitions from the conduction band to empty (hole) states in the valence band for (a1) direct band gap semiconductor and (a2) indirect band gap semiconductor (Tu et al. 1992). Schematic illustration of recombination processes in semiconductor materials: (b) band-to-shallow state transition; (c) recombination at a state deep in the band gap; (d) an Auger recombination process; (e) a multiphonon process (the first and last transitions are shown to be radiative) (Grovenor 1989).

1.2 GaAs Device Basics

The basic building block for semiconductor devices is the p-n junction. As is suggested by its name this device is a juncture between p-type and n-type semiconductor material. The p-n junction diode is a two terminal device.

When n- and p-type materials are brought in contact, electrons will flow from the n-type region to the p-type region and holes will diffuse from the p-type region to the n-type region. As a result of this diffusion an electric field is generated and results in the bending of the bands (figure 1.4(a)). At the junction a potential barrier is formed inhibiting the net flow of electrons flowing from the n-type region to the p-type region and the holes from the p-type to the n-type region.

If a forward bias voltage (V_a) is applied to the p-n junction the barrier (ΔE) is reduced (figure 1.4(b)). It is found that under this forward bias condition the net current that flows across the p-n junction increases exponentially with voltage:

$$I = I_o\left(\exp\frac{qV_a}{kT} - 1\right) \tag{3}$$

If a reverse bias is applied to the p-n junction the barrier is increased (figure 1.4(c)). For a large reverse bias voltage the current in the p-n junction is limited by the reverse current (electron flow from p to n). The sources of the reverse current are the minority carriers in the p and n-regions. Their concentration is independent of the magnitude of the applied voltage but strongly dependent on temperature. The salient feature of the p-n junction diode is its ability to conduct large currents in the forward direction while it blocks current

(a)

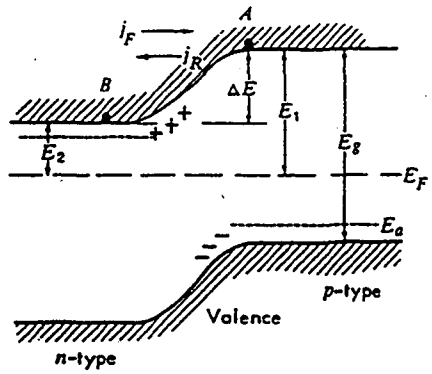

(b)

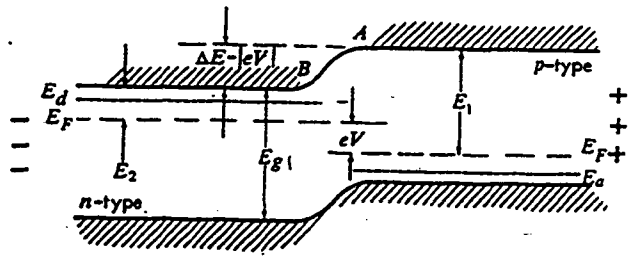

(c)

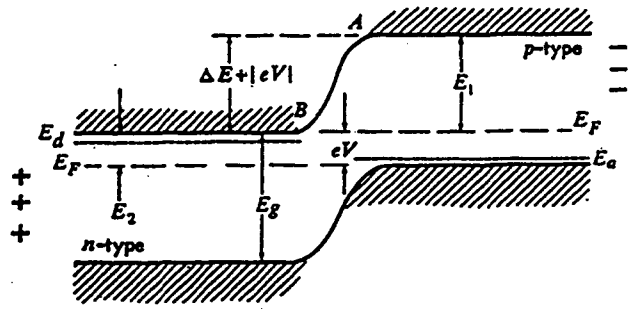

Figure 1.4 Band structure of a p-n junction (a) at equilibrium, (b) under forward applied bias, and (c) under reverse applied bias (Barrett et al. 1973).

flow in the reverse direction. This nonlinearity is widely used to rectify alternating currents.

A light-emitting diode is a p-n junction device which can efficiently convert electrical energy into light (Grovenor 1989). The semiconductor materials chosen for these types of optical applications are selected based on the efficiency of the radiative processes in the material and the wavelength of the light which is emitted.

Since GaAs is a direct band gap semiconductor photons can induce electron transitions without the need of phonon creation and/or annihilation for momentum conservation. Inversely, electron and holes can be injected into a GaAs diode and can recombine to generate photons. It is this efficient photon generation which has made GaAs and its many alloys one of the most important semiconductor materials for opto-electronic applications.

For very high speed device applications (e.g. cellular phones), in order to reduce the transit time of the carriers, high carrier mobilities resulting in high velocities at low electric fields are desirable. This is the second reason why GaAs is preferred over Si. An example of a three terminal device making use of the high GaAs electron mobilities is the n-channel GaAs Metal Semiconductor Field Effect Transistors (MESFET). An n-channel MESFET is shown in following diagram (figure 1.5). In a MESFET, the n-channel is fabricated by epitaxially growing a lightly n-doped GaAs layer on the semi-insulating substrate. Between the metallic gate and the lightly doped n-type layer a depletion region is formed. The depletion region extends partially through the n-channel. The channel current between the source and drain is limited to the width of the undepleted region

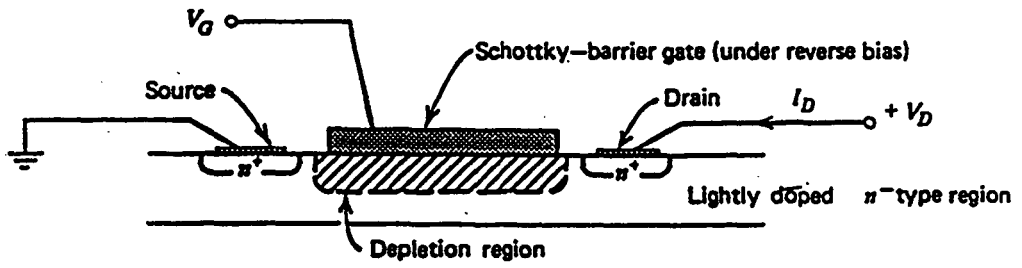

Figure 1.5 Schottky-barrier gate, field-effect transistor. Current flowing from drain to source is modulated by the gate voltage V_g. The source and drain regions are Ohmic and formed by highly doped material (Muller 1986).

between the depleted zone and the substrate. The current flowing through the undepleted region of the channel can be reduced by the applying a reverse bias at the gate electrode. With a sufficiently high reverse bias at the gate, the channel can be completed depleted up to the substrate. Under these conditions, no current would flow through the channel.

In addition to the higher electron mobility in GaAs as compared to Si, the electron peak velocity is also about 1.5 times that of the Si saturation velocity (Swaminathan 1991).

1.3 Solid Phase Epitaxy and Motivation of This Research

As mentioned earlier Solid Phase Epitaxy (SPE) is a crystal growth process in the solid state which can occur when an amorphous layer is in contact with a single crystal substrate. The amorphous layer recrystallizes epitaxially by rearrangement of atoms at the crystalline/amorphous interface. The single crystal substrate serves as a template (Csepregi et al.1975). In the process of turning amorphous semiconductors crystalline SPE also activates dopant atoms which may be located in the amorphous layers. Such a case are ion implanted layers which are both amorphous and doped after implantation. The solid phase epitaxial recrystallization of an implanted layer appears most suitable for achieving excellent crystallinity and high dopant activation.

It has been shown that higher activation of implanted dopants in Si can be achieved when Si is fully amorphized by ion implantation and regrown by solid phase epitaxy (Crowder 1970) than when Si is only damaged but not amorphized. The implanted dopants are electrically activated at lower temperatures in the SPE process than when the target is not amorphous. Lower annealing temperatures are attractive because they

minimize diffusion broadening of impurity concentration profile and they minimize contamination by undesirable impurities. Epitaxial regrowth of Si ion implanted amorphous layers on Si occurs at temperatures around 500°C (Crowder 1971). For <110> and <100>oriented Si, a linear regrowth rate is observed for isothermal anneals. Studies have shown that the epitaxial regrowth of ion implanted (100) Si layers result in almost defect free material (Csepregi et al. 1975).

In compound semiconductors, it has been found that the SPE process is more complicated. During reordering in the semiconductor, the individual constituents must incorporate themselves on the correct lattice sites as the crystalline/amorphous interface proceeds towards the surface. For SPE regrowth of GaAs, a 1:1 Ga:As ratio is required at the crystalline/amorphous interface for perfect epitaxial regrowth to occur. During ion implantation, recoils from the Ga and As atoms display a different energy distribution because of the different masses of Ga and As. This leads to a stoichiometric imbalance at the crystalline/amorphous interface which affects the quality of the epitaxial regrowth. It is believed that the deviation from stoichiometry results in microtwins, stacking faults, and other defect structures (Narayanan and Kachare 1974; Kular et al. 1980; Grimaldi et al. 1982; Bhattacharya et al. 1983). It is the aim of this study to understand the effects of stoichiometry on SPE regrowth.

In order to obtain the proper prospective for SPE we will briefly review standard thermal annealing procedures. Thermal annealing is a process necessary to restore the crystalline lattice to perfect order and to position the dopant atoms on electrically active lattice sites after ion implantation. In the case of GaAs, extended defects can be removed

by annealing at 500°C (~10 min.). Temperatures greater than 700°C, however, are required for the full electrical activation of the implanted ions (Ryssel and Ruge 1986). The optimum annealing conditions for GaAs (Rimini 1995) are higher temperatures (900°C-950°C) and short times (5-10 sec). Figure 1.6 shows the onset of carrier activation for Si and Be implanted GaAs and the relative disorder remaining after annealing at each temperature (Cummings et al. 1986). The doses used in these samples were $1x10^{15}/cm^2$. The standard thermal and rapid thermal anneals were of 10 min. and 5 sec. duration, respectively. The relative disorder remaining was measured by channeling Rutherford Backscattering Spectrometry (RBS). The electrical activation was determined from Hall measurements. The optimal annealing conditions occur at high temperatures which can lead to dopant redistribution.

Stoichiometry can have a strong effect on the lattice site occupation of dopant atoms. One method used to increase the electrical activation of C implanted in GaAs is the use of dual implants also called co-implants. Dual implants with one dopant species and one crystal sublattice species help in forcing the implanted impurities to one sublattice in the III-V compound (Malik 1988). Implantation of C in GaAs leads to an excess of atoms on the As sublattice only, resulting in non-stoichiometry. The 1:1 ratio of Ga:As is no longer maintained. Heckingbottom (Heckingbottom et al. 1973) proposed matched dual implants to circumvent this stoichiometry problem. The authors suggested that when a dopant is implanted for one sublattice of an AB compound, an equal amount of the host atom of the other sublattice should also be implanted. Hence, the energy and the dose of the dual implant is chosen so that the concentration distribution of the dual implant

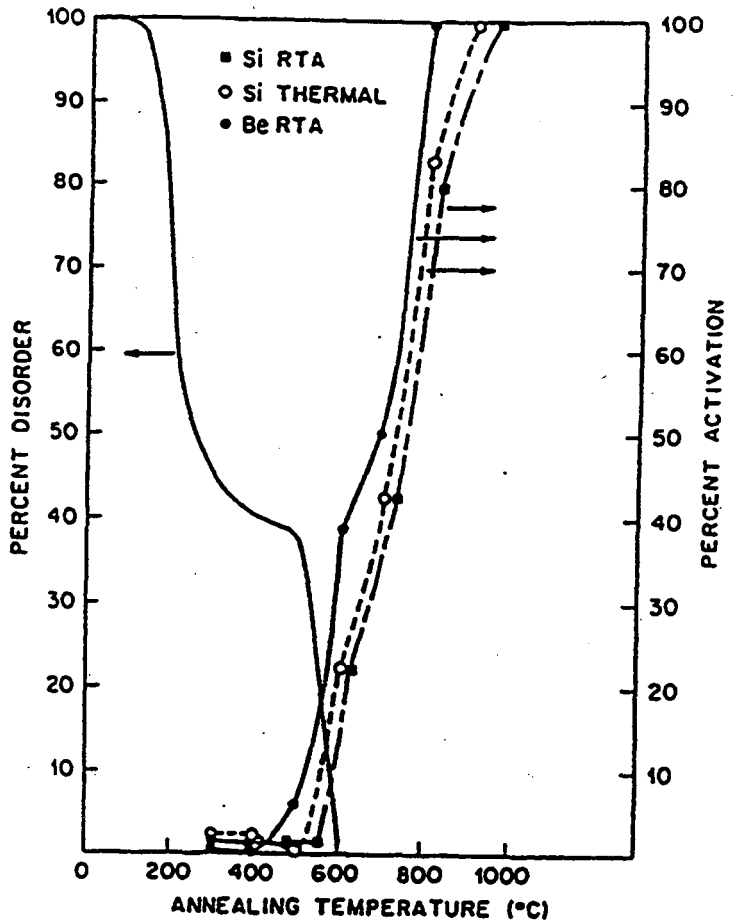

Figure 1.6 Carrier activation in Si- and Be-implanted GaAs ($1x10^{15}/cm^2$ after rapid thermal annealing or furnace annealing. Relative disorder remaining after annealing as measured by channeling RBS is also shown (Cummings et al. 1986).

quantitatively matches that of the dopant atom. In this manner, both sublattices are built up equally. For C implanted in GaAs in order to improve the C substitution in the As sublattice and become acceptors, a group III atom has to be co-implanted to build up the Ga sublattice.

The type of substitutional site occupied by an amphoteric dopant and its electrical activity are influenced by the kind of point defects which are available. Specifically, the type and concentration of vacancies are determined by the local stoichiometry and the damage. Moll et al. (Moll et al. 1992) found that the co-implantation played a dual role in the increase of the electrical activation of C. They found that it is essential that the co-implant create sufficient damage and maintain stoichiometry to obtain maximum electrical activation. The larger damage resulting from the co-implant leads to a higher concentration of As vacancies. As a result, the C can move to As sites. The authors also observed that maintaining the stoichiometry reduced the concentration of compensating native donors and increased the electrical activation. As stated previously, dual implants confined the implanted impurities to the specified sublattice and decrease the effects of self-compensation. Since, it was unclear to what degree the improvement in electrical activation was due to the additional damage or the stoichiometry, a systematic study was performed on various ion species co-implanted with C at room temperature (Morton et al. 1995). In this work, Ar, Ga, As, and Kr ions at doses of $5x10^{13}/cm^2$ and $5x10^{14}/cm^2$ and various dose rates were co-implanted with C. The authors observed that for each dose and a given dose rate the maximum sheet carrier concentration was obtained with the Ga co-implants.

In the research presented here, the effect of local stoichiometry on the solid phase epitaxial regrowth of GaAs was studied in a systematic manner. Both Ga and As ions were implanted into GaAs sequentially to create an amorphous GaAs layer which was locally stoichiometric. The SPE process of these layers was studied. By implanting only Ga and As into GaAs any impurity effects were eliminated. Also, by implanting Ga only, As only, or co-implanting Ga and As, a medium was provided to determine if the poor recovery of ion implanted GaAs was due to the damage or the stoichiometry.

The objective of this research was to understand the role of stoichiometry in the SPE regrowth of ion implanted GaAs. By understanding the epitaxial process, it may become possible to determine implant conditions which could lead to greater electrical activation of ion implanted III-V layers.

1.4 Previous Studies of SPE in GaAs

Due to the different masses of the constituents of a compound semiconductor, the maximum energy transfer and the recoil ranges of each element are different. As a result, implantation leads not only to damage as in elemental semiconductors but also to a distribution of Ga and As which deviates from stoichiometry. The heavier host element (As atomic mass 75) is displaced less than the lighter host element (Ga atomic masses 69 and 71) leading to these deviations from stoichiometry.

Two of the problems encountered with the SPE regrowth of III-V compound semiconductors are the evaporation of group V elements at temperatures greater than 500°C and the formation of residual defects.

In addition, there are stoichiometry problems associated with amphoteric dopants. In the case of amphoteric dopants in GaAs (e.g. Si), the dopant atoms can, in principle, sit on either sublattice. This is a problem when one wishes to introduce a dopant onto a specific sublattice, and create either a p-type or a n-type layer. If the dopant resides on the wrong sublattice, it will form compensating centers. As a result, the electrical activation of the implanted layer will decrease due to the compensation. Hence, the substitutional lattice site occupation of an impurity is not a sufficient condition for the electrical activity of the implanted layer.

A further problem of technological importance is the inability to activate high dose n-type implants in GaAs. This phenomenon has been attributed to the point defects which remain after annealing. This is of fundamental interest since n-type GaAs is an attractive semiconductor material for high speed devices due to the high mobility of electrons. The relationship between the solubility of implanted dopants in GaAs and their electrical activity has been studied for certain dopants (Pearton et al. 1987). For example, Te implanted in GaAs to a dose of $10^{16}/cm^2$ and laser annealed, showed 90% of the dopant atoms on substitutional lattice sites (as measured by channeling) (Barnes et al. 1979), although less than 20% of the implanted atoms were electrically active. This was ascribed to the presence of native defect complexes. As a result, this work shows that the substitutionality of a dopant atom in ion implanted GaAs is not a sufficient condition for its electrical activity. The presence of native defects (e.g. anti-site complexes, vacancies, etc.) can compensate dopants and reduce the free carrier concentration.

2. Radiation Damage

2.1 Ion Implantation

The ion implantation technology is widely used for doping semiconductors. Some of the advantages of ion implantation include: control of doping level, control of implanted thickness layer, choice of dopant profile (good uniformity), and high throughput. In addition, selective regions of the substrate can be implanted by using masking materials. One of the most significant advantages of ion implantation is that it is a "low" temperature process (relatively speaking) which limits the diffusion of the implanted species. Currently, one of the foci of ion implantation research is to devise better methods to activate the implanted dopants and remove the damage, while minimizing the amount of dopant diffusion.

Ion implantation is also applicable to device isolation. In this case the technology is used to form high resistivity regions in substrates. The implantation leads to regions which are highly damaged. Deep level centers are formed which trap free carriers and carrier mobilities are decreased.

Energy loss processes determine the final penetration depth of a projectile into the solid and the amount of lattice disorder produced. There are two types of energy loss processes, electronic and nuclear energy loss. Electronic energy loss involves the interaction between the incident ions and the electrons of the host material. Owing to the small masses of the electrons, electronic collisions lead to a negligible deflection of the ion trajectory. Nuclear energy loss involves the nuclear interaction between the incident ions

and the atoms of the host material. Nuclear collisions result in large angle deflections of the ion trajectory and displacements of the target atoms resulting in crystalline damage in the target.

The range and distribution of implanted ions can be calculated accurately by the Lindhard, Scharff, and Schiøtt (LSS) theory. This theory has been reviewed in detail in the literature (Malik 1988). This theory finds that nuclear stopping is more important than electronic stopping for heavy ions and at lower energies. On the other hand, electronic stopping is more important for lighter ions and higher energies. Figure 2.1 illustrates the dependence of the nuclear and electronic energy loss rate on the energy of the projectile. From the figure, it can be denoted that nuclear collisions dominate at low energies and electronic collisions at higher energies. Table 2.1 reports values for the characteristic energies E_1 and E_2 shown in the figure (Mayer and Lau 1990). In the energy range where nuclear stopping dominates lattice atoms are displaced. Nuclear stopping is usually treated as a classical elastic collision problem between charged particles with an appropriate screening factor to take into account the surrounding electrons. Over the range considered, nuclear stopping is generally not a strong function of the energy of the projectile. For an amorphous target, nuclear stopping results in a distribution of implanted ions which is to a first approximation gaussian. The atomic density of the implanted atoms as a function of depth is given by LSS:

$$n(x) = \frac{\varphi}{\sigma_p \sqrt{2\pi}} \exp\left[\frac{-(x - R_p)^2}{2\sigma_p^2}\right] \tag{4}$$

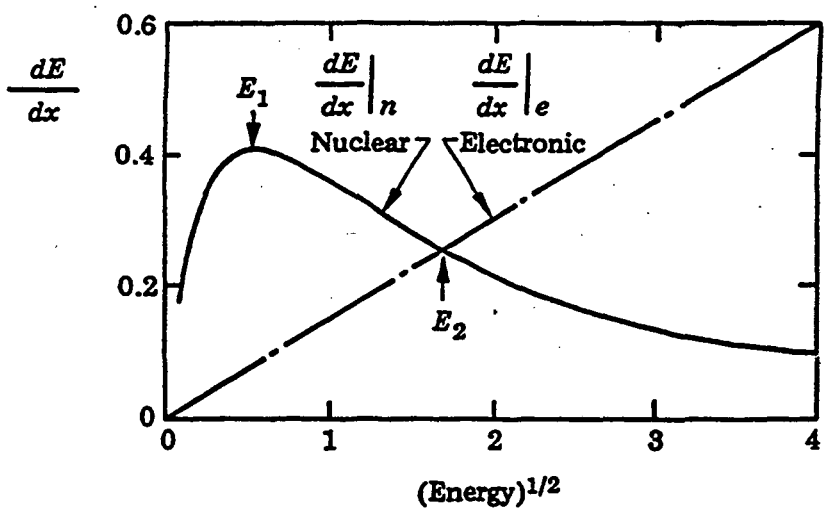

Figure 2.1 Rate of energy loss (dE/dx) versus (energy)$^{1/2}$ showing nuclear and electronic loss contributions (Mayer 1990).

Ion	E_1 (Si)	E_1 (GaAs)	E_2 (Si)	E_2 (GaAs)
B	3	7	17	13
P	17	29	140	140
As	73	103	800	800
Sb	180	230	2000	2000
Bi	530	600	6000	6000

Table 2.1 Characteristic energies E_1 and E_2 corresponding to the maxima in nuclear and electronic energy loss distributions in figure 2.1 (Mayer 1990).

where φ is the implanted dose (atoms/cm^2), σ_p is the standard deviation in the projected range, and R_p is the projected range. The above distribution assumes that the target is amorphous and ignores any channeling effects. The projected range depends on the velocity of the ion and the stopping power of the substrate material. For implants of a given incident energy, a high mass ion (low velocity) will come to rest closer to the surface, whereas, a lower mass ion (high velocity) will have a larger penetration depth.

Some further issues that must be addressed with ion implantation are channeling and beam annealing. Channeling occurs in a single crystal when the ion beam is aligned with an axis of the crystal and is steered into the open spaces (Tesmer et al. 1995). The steering is due to the small-angle screened Coulombic collisions between the ions and the host atoms along the channel. Channeling results in a non-Gaussian implant profile (e.g. long tail). To avoid channeling the crystal is generally misaligned, so that the ions are incident in a nonchanneling direction. In this manner, the crystalline target approximates an amorphous target. High dose rates can lead to a substantial rise in target temperature due to the high power injection into the specimen by the ion beam. The temperature of the implant is crucial because it affects the diffusion of both the implanted ions and the defects.

2.2 Defects in Semiconductors

It is essential to understand defects because they introduce electronic states in the band gap of the semiconductor. Defects and crystalline disorder also lead to increased scattering of charge carriers which result in a higher resistivity and lower mobility. In addition, defects can interact with the dopants during thermal processing and affect the

electrical activity of the dopants. Consequently, residual defects can affect the overall electrical activation of the implanted ions and affect the properties of the devices.

Defects have been reviewed and discussed in detail in the literature (see for example Rimini 1995). There are three fundamental types of defects, vacancies, self interstitials, and anti-sites. These are point or 0-D defects. A vacancy-interstitial pair is called a Frenkel defect, and a vacancy alone is called a Schottky defect. In compound semiconductors, there are two types (cation and anion) of vacancies, interstitials, and anti-sites. Point defects can form complexes amongst themselves (i.e. divacancies). Other defects which are present as a result of annealing an implanted layer are dislocations (line or 1-D defects); stacking faults, twins, grain boundaries (planar or 2-D defects); and precipitates and voids (volume or 3-D defects). Extrinsic stacking faults result from the clustering of self-interstitials. Whereas, intrinsic stacking faults are due to the clustering of vacancies. Dislocations are non-equilibrium defects. After implantation and annealing, dislocations can form dislocation networks and dislocation loops. These defects can be detrimental especially if they are located within an electrically active region.

The primary types of implantation induced damage are (1) isolated point defects or point defect clusters, (2) local amorphous zones, and (3) a continuous amorphous layer. These types of radiation damage will be discussed in the next section.

2.3 Radiation Damage in Semiconductors

During implantation, nuclear collisions between target atoms and incident ions lead to displacement of host atoms. If the energy transferred is large enough, it will result in a cascade of displacements or amorphous zones. If the dose is large enough, these

amorphous zones will overlap and a continuous disordered layer (amorphous layer) will be created (Wesch et al. 1989).

An important characterization parameter of the radiation damage is the number of vacancies created in the target per incident ion. In ion implantation, the energy deposited in nuclear collisions is a measure of the damage primarily produced during bombardment. The defects created are determined by the energy deposited into nuclear processes, because such collisions can transmit enough energy to displace host atoms and create vacancies (Wesch et al. 1989). The primary defects produced are Frenkel pairs. In addition to Frenkel pairs, upon annealing point defect clusters and extended defects can form (Jones et al. 1988). Figure 2.2 illustrates the varieties of defects which can be created during implantation.

Radiation damage in semiconductors has been studied extensively (Rimini 1995). For ion energies greater than the displacement energies the knock-on atom leaves the lattice site. These are called primary collisions. In Si, the displacement energy is about 14 eV. These knock-on Si atoms can recoil and collide with other atoms which in turn are called secondary collisions. This sequence of collisions and displaced atoms results in a collision cascade. In the cascade process atoms are ejected from the center of the cascade leaving a zone rich in vacancies and a surrounding region rich in interstitials. Depending on the target temperature, some reordering can occur by local diffusion of point defects. At low doses (less than $10^{12}/cm^2$), bombardment with heavy ions results in individual isolated damage regions around each ion track with a very small probability of cascade overlap. In the case of high doses (greater than $10^{14}/cm^2$), complete overlap of damage

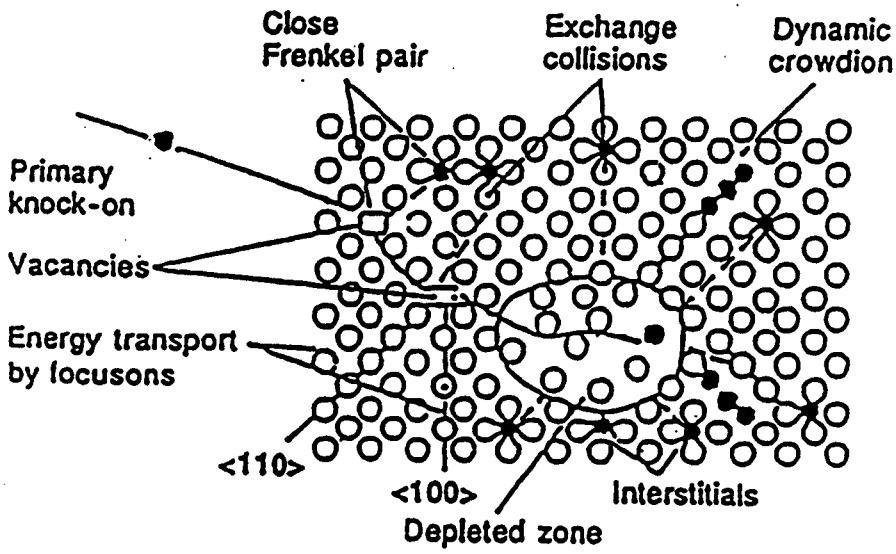

Figure 2.2 Varieties of defects created by ion implantation (Mayer 1990).

regions occurs. As a consequence, a continuous amorphous layer is formed. Beyond the crystalline/amorphous interface, isolated damage regions are formed called "end of range" damage. Figure 2.3 illustrates the damage upon bombardment with heavy ions at low doses and heavy doses.

As stated previously, the displacement energy for Si can be estimated from the threshold energy for electron damage to be about 14 eV (Bauerlein 1962). The damage distribution can be calculated using the deposited energy density. Using the modified Kinchin-Pease relation (Kinchin et al. 1955), the total number of displacements in the implanted volume is given by:

$$N_d = \frac{0.8\int_0^\infty \nu(E,x)dx}{2E_d} \tag{5}$$

where E_d is the displacement energy, ν(E,x) is the nuclear deposited energy distribution, and 0.8 is a correction factor. This model assumes that the average energy required to displace an atom is $2E_d$. Upon calculation of the damage distribution, it is observed that the vacancy depth distribution is different than the implanted ion distribution. The vacancy distribution is considerably shallower than the projected range of the implanted ion. This is due to the fact that the ions come to rest beyond the range in which they displace the atoms.

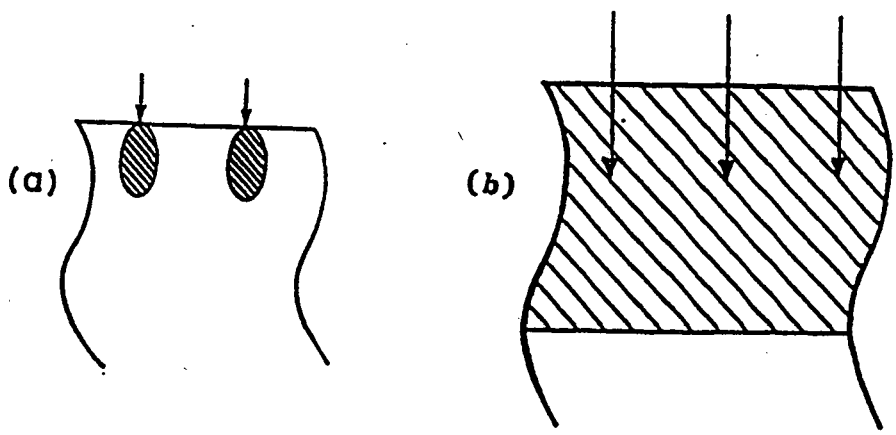

Figure 2.3 Damage produced by bombardment of heavy ions for (a) low doses and (b) high doses (Rimini 1995).

2.4 Ion Implantation Damage and Amorphization of GaAs

During ion implantation, if sufficient energy is deposited into nuclear collisions a phase transformation from crystalline to amorphous will take place. One model used to describe the amorphization process is the critical damage energy density (CDED) model (Stein et al. 1972). The threshold damage density (TDD) is the amount of nuclear deposited energy required for amorphization. Values of TDD derived from 20 keV Si (dose of $1x10^{15}/cm^2$, LN_2 implant) implantation into Si and GaAs were reported as $1.6x10^{20}$ keV/cm^3 and $3.3x10^{20}$ keV/cm^3, respectively (Jones et al. 1991). According to the CDED model, a lattice will spontaneously relax into an amorphous state when there is a large enough density of defects.

Another amorphization model involves overlapping of amorphous zones, until full amorphization is obtained. As the number of ions is increased, the individual damage clusters overlap to form a continuous amorphous layer. Figure 2.4 shows the dose dependence of lattice disorder for 120 keV Se in GaAs implanted at room temperature. The amount of damage was determined from Rutherford Backscattering Spectrometry measurements. From the figure, it can be observed that at a dose of $5x10^{13}$ ions/cm^2 complete overlap occurs and an amorphous layer is formed.

The critical dose for amorphization depends on the ion mass and the implant temperature (Wesch et al. 1989). As the ion mass is decreased, the critical dose for amorphization increases because there is less nuclear deposited damage per ion. Critical doses for amorphization increase as the implant temperature increases. For low

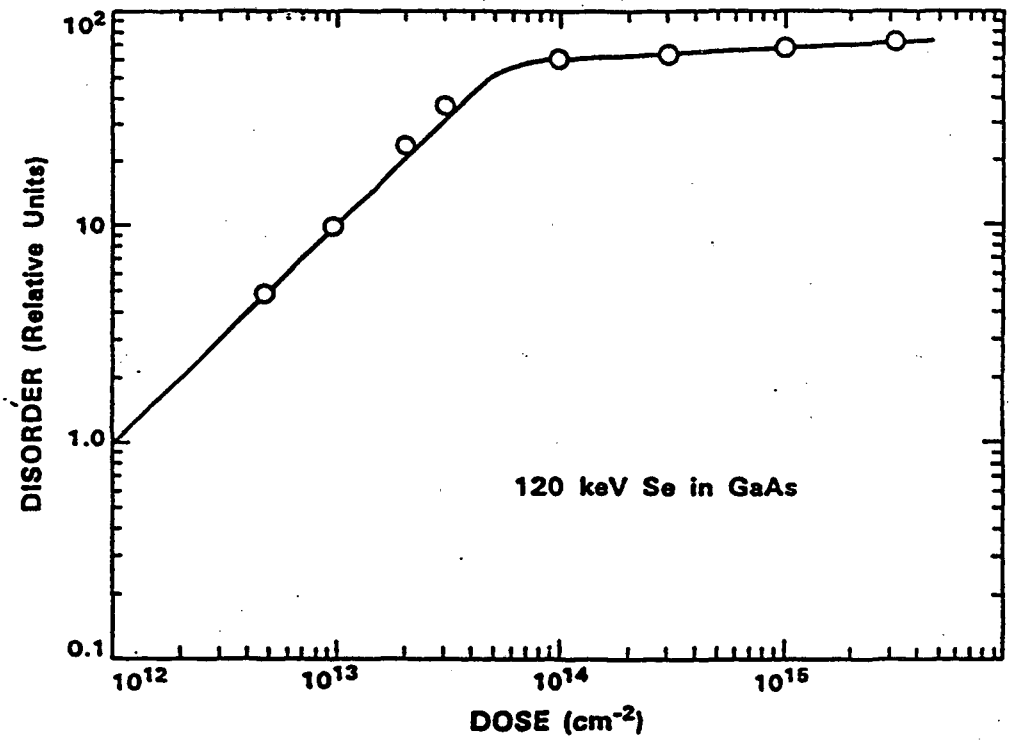

Figure 2.4 The dose dependence of the lattice disorder as measured by channeling RBS produced by 120 keV Se implantations at room temperature (Bhattacharya et al.,1982)

temperature implants (e.g., LN_2) the damage is "frozen in". The low temperature limits the mobility of point defects suppressing self-annealing. Whereas, in room temperature implants the damage decreases due to defect annealing. This has been discussed in the literature (Rimini 1995). In the case of light ions, for implantation at high substrate temperature (i.e., higher than room temperature) the defect concentration may never reaches the critical defect concentration to produce the amorphous phase. As a consequence, at higher implant temperatures a higher energy deposition is required to create an amorphous layer than at lower implant temperatures

Summarizing there are two proposed mechanisms for amorphization. In the first model discussed amorphization occurs by damage accumulation. When the material reaches a critical threshold defect concentration the material becomes amorphous. The other proposed model assumes that each ion produces a roughly cylindrical track of amorphous material along its track. A continuous amorphous layer is achieved when amorphous regions overlap.

Table 2.2 shows the critical doses for the formation of amorphous layers for several elements implanted in Si, GaP and GaAs at room temperature (Ryssel and Ruge 1986).

Semiconductor	Element	Mass of the main isotope	Ion Energy (keV)	Dose (cm^{-2})
Si	B	11	200	$8x10^{16}$
	P	31	200	$6x10^{14}$
	Sb	122	300	$1x10^{14}$
GaAs	Zn	64	70	$3x10^{13}$
	Cd	114	60	$3x10^{13}$

Table 2.2 Critical doses for the formation of an amorphous layer in Si, and GaAs at room temperature (Ryssel 1986).

2.5 Transport of Ions In Matter (TRIM)

TRIM (Ziegler et al. 1985 and 1980) is a computer simulation program used to calculate the distribution of the implanted ions, the energy deposition, and the damage profiles for energetic ions in solids. TRIM allows theoretical predictions over a wide range of parameters.

There are two methods for simulating the ion bombardment in solids. Both of which have been reported in the literature (Rimini et al 1995). The two methods are the binary collision approximation (BCA) and the molecular dynamics (MD). Only the BCA method will be discussed here because TRIM is based on this method. The BCA method is also called the Monte Carlo method, because a random selection process is used for each collision throughout the program. If the target structure is assumed to be random, the next collision atom for the incoming ion is found from a random selection process.

In the Monte Carlo Method the individual collision cascades are simulated. The results are averaged from several hundred cascades. The Monte Carlo program follows the collisions that individual ions undergo while in motion. Some important parameters used in the simulation program are the displacement and the binding energies. The displacement energy is the amount of kinetic energy that the target atom must receive to leave its lattice site and form a stable interstitial (Frenkel pair). The binding energy is the amount of energy by which a target atom is bound to the lattice site. The values for these parameters are not well established. The displacement energies obtained from the

literature for Ga and As in GaAs are 9.0 eV and 9.4 eV, respectively (Haynes and Stoneham 1985).

The TRIM procedure has been discussed by Dresselhaus et al. (Dresselhaus et al. 1992). The method is as follows: (1) an ion is shot in, (2) the ion collides with a target atom, (3) the program calculates the kinematics of the collision, (4) it follows the trajectory of the recoiling target atom, since the recoil atoms can displace other atoms, (5) after all recoil atoms fall below a certain energy, the program goes back to the original ion, (6) it repeats the above procedure until the ion energy falls below the displacement energy and it can not displace any more atoms, and (7) it proceeds to the next incident ion. Usually the simulation is done for over 1000 incident ions. The incident ions are assumed to change trajectory at each elastic collision with the target atom and to move in straight free path between collisions. Nuclear collisions result in large energy losses and significant angular deflection of the trajectory of the implanted ion. Lattice disorder in semiconductor crystal is attributed to the nuclear collisions. Electronic collisions involve much smaller energy losses per collision and negligible deflection of ion trajectory. Consequently, lattice disorder due to the electronic collisions is negligible. The distribution of the deposited energy density into nuclear collisions can be converted into a damage distribution, assuming only recoils receiving an energy greater than the displacement energy are displaced. The energy transfers which are less than the displacement energy generate phonons. One of the disadvantages of TRIM is that it overestimates damage. It does not take into account annihilation of defects.

A TRIM simulation is shown for 185 keV Ga ions implanted in GaAs in figure 2.5.

From the simulation, it can be noted that the damage distribution due to nuclear energy loss of the ions has a peak at a shallower depth than the distribution of implanted ions.

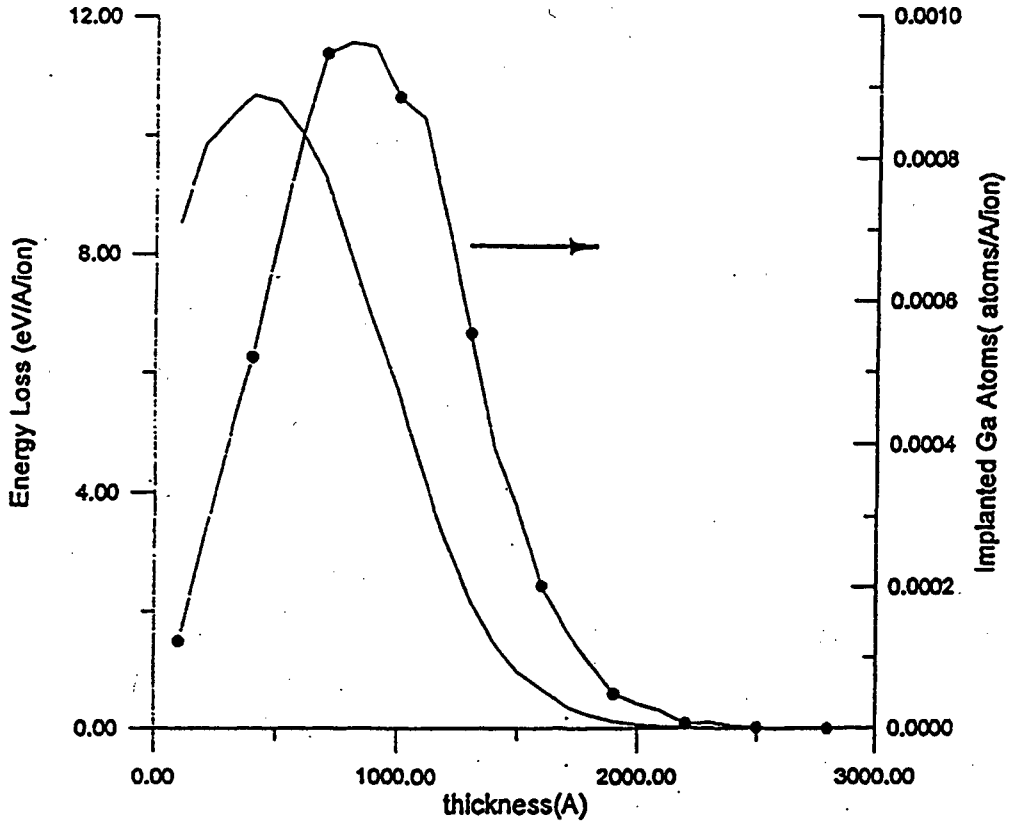

Figure 2.5 TRIM simulation for 185 keV Ga ions implanted in GaAs. The nuclear energy loss distribution and the implanted range of Ga ions are shown.

3. Fundamentals of Solid Phase Epitaxy

A phase transformation occurs when it is thermodynamically advantageous and kinetically possible to reconfigure the materials. Solid phase epitaxy is a solid state transformation from the amorphous to crystalline phase. The driving force for the amorphous to crystalline transition is the lowering of the free energy of the material.

3.1 Regrowth Kinetics in Si

Solid phase epitaxial regrowth occurs in Si at about 500°C. The amorphous layer recrystallizes by a movement of the planar crystalline/amorphous interface. Dopants become partially or totally activated as they get incorporated into the advancing recrystallized region. The regrowth velocity v_g is given by:

$$v_g = v_0 \exp\left(\frac{-E_a}{kT}\right) \tag{7}$$

where v_o and E_a are the prefactor and activation energy, respectively. Figure 3.1 illustrates solid phase epitaxial regrowth Si layer amorphized by Si implantation on <100> Si. The total dose was $8x10^{15}/cm^2$ and implants were done at LN_2 temperature. The initial amorphous layer thickness was approximately 460 nm . The samples were preannealed at 400°C for 60 min., then annealed at 500°C for various annealing times.

Reported values of the activation energy for the SPE process of amorphous Si layer created by Si implantation in Si vary from 2.76±0.05eV (Olson and Roth 1988) to 2.35±0.1eV (Csepregi 1978). It is interesting to note that the recrystallization of amorphous layer is strongly orientation dependent as demonstrated in figure 3.2. An Arrhenius plot of the regrowth velocities for the different orientation shows that SPE in all

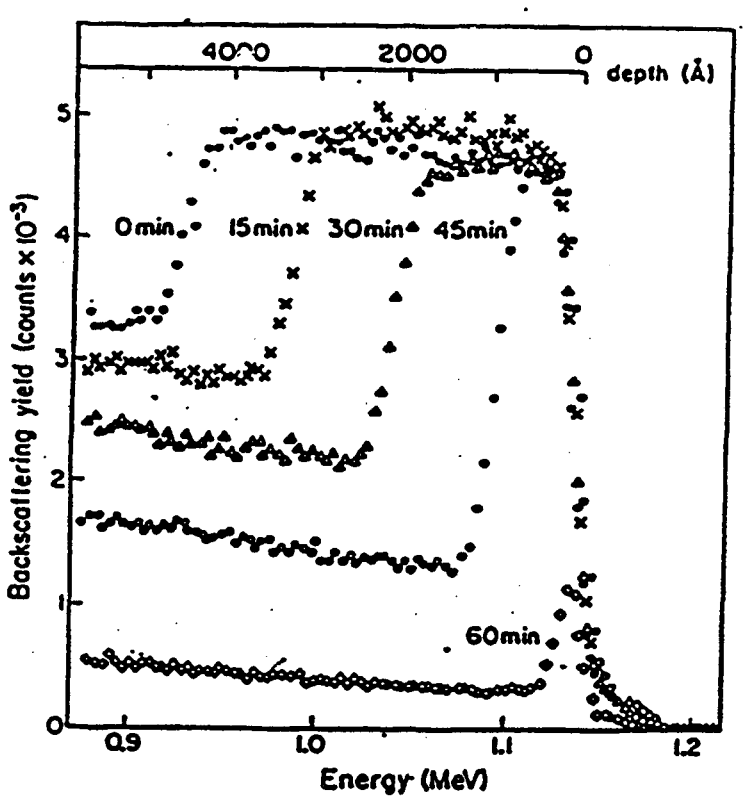

Figure 3.1 SPE regrowth of <100>Si self-implanted with Si. The total dose was $8x10^{15}/cm^2$ and the implant was performed at LN_2 temperatures. The samples were annealed at 500°C for various time intervals (Csepregi 1978).

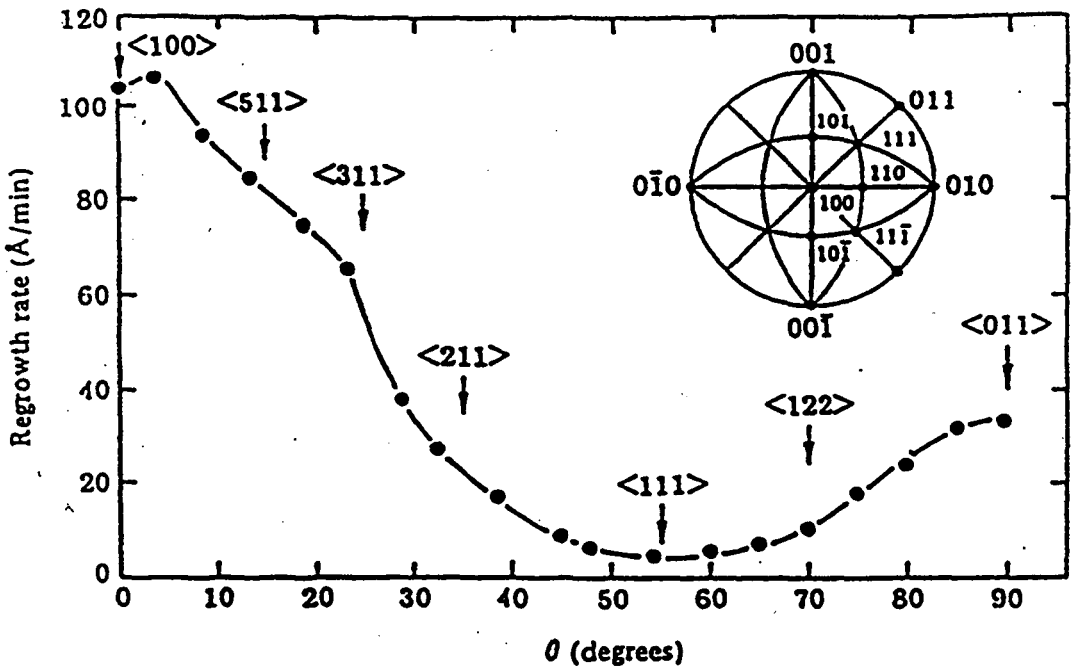

Figure 3.2 SPE regrowth rates of Si self-implanted with Si for various orientations (Mayer 1990).

orientations have the same activation energy but significantly different prefactors (e.g. very different regrowth velocities). For the <110> and <100> oriented Si, a linear regrowth velocity has been reported (Csepregi et al. 1977). The authors observed a nonlinear regrowth velocity for the <111> oriented Si.

Csepregi et al. (Csepregi et al. 1975) observed in Si implanted in <111> Si, that the regrown layer contained a high density of defects. Transmission Electron Microscopy (TEM) showed stacking faults and microtwins. Twin boundaries are planar defects. At the twin boundary, there is a misorientation of the lattice. Twinning in ion implanted GaAs has been extensively reported (Rimini 1995). In the (111) orientation it is necessary to simultaneously attach three adjacent atoms from the amorphous phase to a crystalline atom for a growth step. The three atoms can add in the correct lattice positions or with a twin orientation.

3.2 Regrowth Kinetics in GaAs

Annealing is required for the dopants to become electrically active and to restore crystalline order. Post implantation annealing temperatures of about 800-950°C are generally required for GaAs to minimize residual damage and to achieve electrical activation of implanted ions.

Three annealing stages have been observed in amorphous GaAs (Sealy 1988; Kular et al. 1980). Stage I occurs at temperatures between 150-400°C, in this temperature range recrystallization takes place leaving behind microtwins and stacking faults. Stage II occurs at 400-500°C. During this stage, microtwins and stacking faults are annealed out.

Stage III occurs at temperatures greater than 700°C. Dislocation loops are annealed out above this temperature.

In GaAs, it has been observed that heavily damaged amorphous layers are harder to regrow by solid phase epitaxy (Williams et al. 1980). It was postulated that good crystalline quality material could be obtained depending on the implant conditions and the annealing temperatures. In the study by William et al. Ar^+ was implanted into (100)GaAs at two doses. The low dose and high dose were $5x10^{13}/cm^2$ and $2x10^{14}/cm^2$, respectively. The implants were done at LN_2 temperature. The channeling spectra for the epitaxial regrowth of the two samples are shown in figure 3.3. At the lower dose good epitaxial quality was achieved after annealing at 180°C for 10 minutes. The SPE behavior for the lower dose sample is similar to the SPE observed in Si, namely a planar crystalline/amorphous interface advancing to the surface. For the sample implanted with the high dose, annealing temperatures of 600°C were required to obtain good crystalline quality. From the RBS spectra from the sample annealed at 250°C, it appears that the crystalline/amorphous interface is nonplanar during SPE.

Gamo et al. (Gamo et al.1977) have suggested that the difference in regrowth behavior between Si and GaAs is attributed to the local variations in stoichiometry in the implanted regions in GaAs. At the low temperatures where reordering takes place, the temperatures are insufficient to allow for the diffusion of the Ga and As, necessary to adjust the local stoichiometry.

A marked dependence of the regrowth quality on the initial amorphous layer thickness has been observed in GaAs (Grimaldi et al. 1981). The authors determined that good quality regrowth of very thin (40 nm) GaAs amorphous layers could be achieved.

They found that the number of extended residual defects after annealing increased linearly with the initial amorphous thickness.

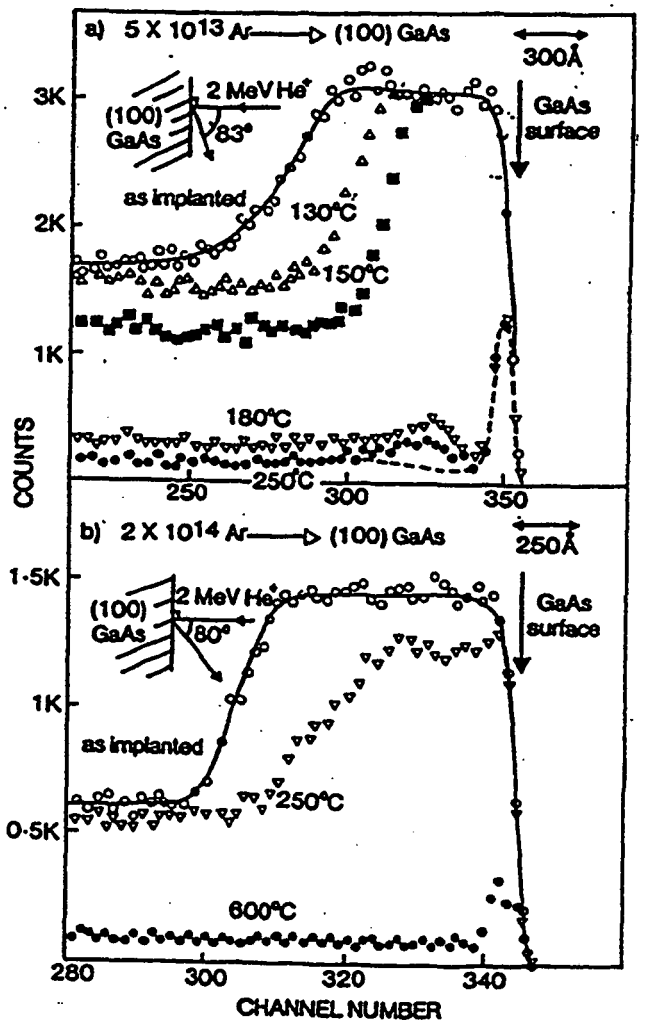

Figure 3.3 Isochronal annealing of (a)$5x10^{13}$ Ar/cm^2 and (b)$2x10^{14}$ Ar/cm^2 implanted (100)GaAs. The 130°C anneal in (a) is for 15 min, all others are for 10 min. duration. The dotted curve in (a) is for unimplanted GaAs. The GaAs was encapsulated for the 600°C anneal in (b).

4. Influence of Implantation Parameters on Damage Distribution

Parameters which affect the properties of the ion implanted layers include ion mass, ion dose, ion energy, implant temperature, stoichiometric imbalances, capping and annealing temperature. The influence of implantation parameters on the kind and concentration of defects is more pronounced in compound semiconductors than in elemental semiconductors.

Wender et al. (Wender et al. 1989) observed that for weakly damaged (not amorphous) ion implanted GaAs at high dose rates, the concentration of anti-site defects and vacancies increase. In addition, the trapping of mobile interstitials is more likely to occur at higher doses. As a result, the formation of defect complexes is more probable. Moore et al. (Moore et al. 1990) observed that the electrical activation of Si implanted into GaAs (room temperature implant) at a dose of $10^{14}/cm^2$ depended strongly on the dose rate. For a given dose, the defect concentration increases with increasing dose rate. Figure 4.1 illustrates how the dose rate effects the damage for room temperature implants of Si in GaAs. Increasing the dose rate increases the number of defects and their interactions resulting in an increase of damage. It is interesting to note, that at LN_2 implant temperatures the amount of damage does not depend on dose rate. This is attributed to the fact that at low temperatures the point defects are "frozen in". At very low temperatures the point defects are not mobile.

In GaAs, a strong dependence of the amount of damage on implant temperature has been observed. Since, the mobility of defects is temperature dependent, the creation

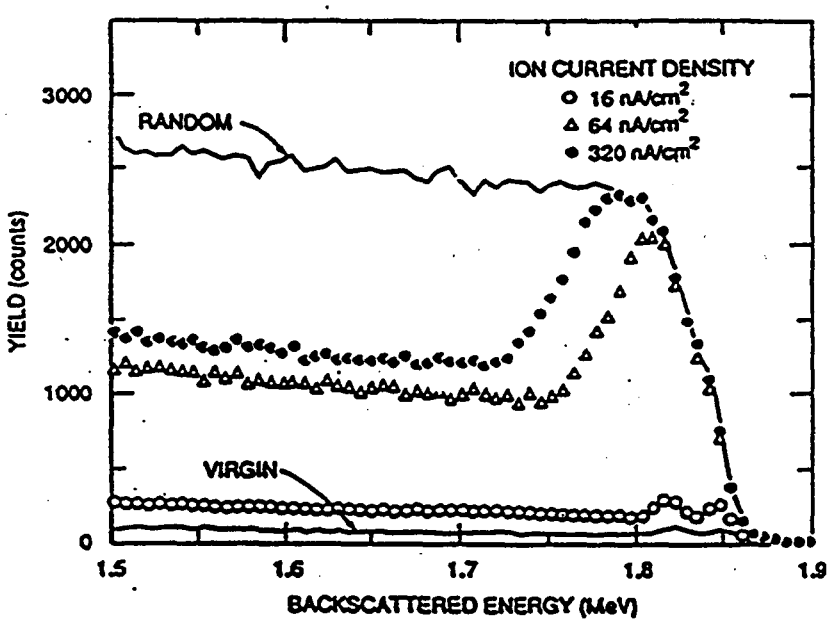

Figure 4.1 Dose rate effects of the damage of Si implanted in GaAs at room temperature.

of stable damage and the formation of an amorphous layer is also temperature dependent. In ion implanted GaAs at room temperature, a significant reduction in the concentration of defects is observed compared to LN_2 temperature implants. This is due to annealing and transformation of the defect structure at room temperature. Dynamic annealing, annealing at room temperature, leads to the diffusion and annihilation of Frenkel pairs. It is believed that dynamic annealing decreases the degree of damage (figure 4.2), and alters the nature of the damage structure by the formation of defect complexes.

For room temperature implants if the dose rate is too high, heating effects can become important and the amount of damage may decrease with increasing dose rate. Poate et al. (Poate et al. 1984) suggested that high temperature implants and high dose rate implants can lead to the formation of dislocation loops and defect clusters. The authors observed that these defects were much harder to anneal than a continuous amorphous layer. These point defects annihilate or associate into more complex defects such as divacancies, and clusters of two or more interstitials. As a result, room temperature implants are harder to anneal than LN_2 temperature implants.

It has been observed that amorphous layers produced by LN_2 temperature implants are more easily reordered than similar layers produced by room temperature implants (Williams et al. 1980; Wrick et al. 1981). For the LN_2 temperature implants, the crystalline/amorphous interface is more abrupt. As a result, a more perfect seeding for the regrowth can lead to a better crystallization.

The energy of the implant species is also an important parameter. Krynicki et al. (Krynicki et al. 1991) found for Cd implanted in GaAs at room temperature, as the ion

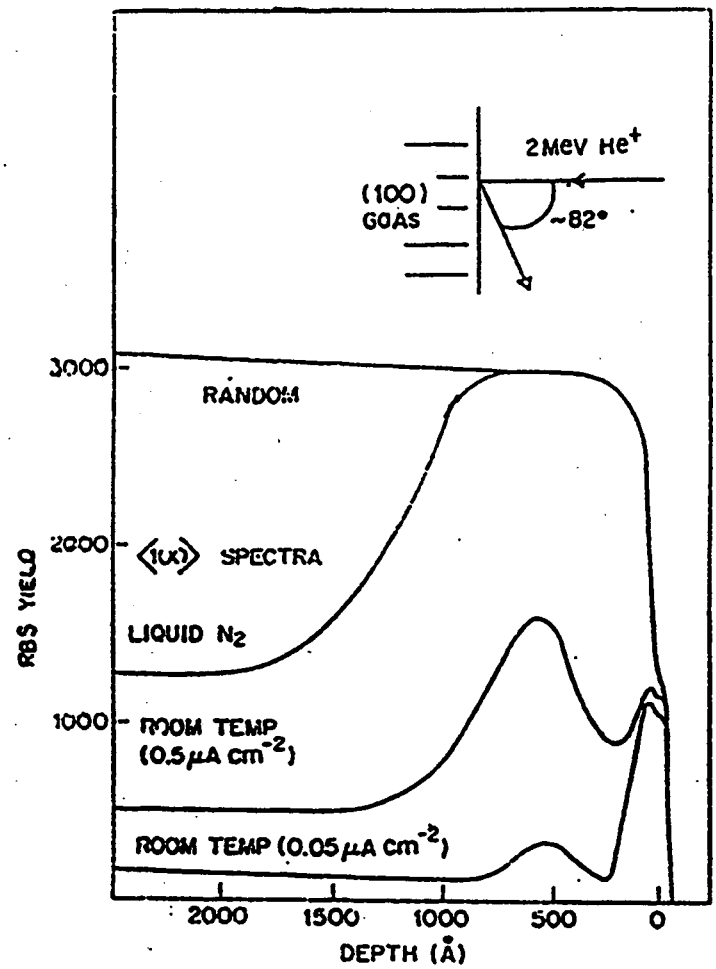

Figure 4.2 RBS spectrum for 100 keV Ar implanted in GaAs to a dose of $8 \times 10^{13}/cm^2$ at implanted at LN_2 and room temperature (Poate et al. 1984).

energy decreased the critical energy density (CDED) for amorphization increased as illustrated in table 4.1. The authors suggest that a higher CDED is required at lower implant energies because the defects are closer to the surface. As a result, for room temperature implants the defects can diffuse to the surface and annihilate. Hence, a higher CED is needed for lower energy implants of Cd into GaAs at room temperature.

Energy (keV)	Critical Energy Density (eV/cm^3) $x10^{23}$
20	1.75
40	1.80
80	1.47
120	1.15
180	0.55

Table 4.1 Values of critical energy density for amorphization as a function of implant energy for Cd implanted in GaAs at room temperature (Krynicki et al. 1991)

5. Characterization Techniques

5.1 Rutherford Backscattering Spectrometry (non-channeled and channeled)

5.1.1 Basic Principles of Rutherford Backscattering Spectrometry (RBS)

For RBS typically a Van de Graaf accelerator is used to produce a He^+ ion beam in the MeV energy range. The high energy beam (1-2 MeV) of monoenergetic collimated light ions (H^+, He^+) is directed towards the sample. A small number of the light ions are backscattered and are detected by a solid state detector that measures the energy of the particles. Some of the applications of RBS include: accurate determination of stoichiometry, elemental aerial density, and impurity distributions in thin films.

Some of the advantages of this technique include the following: (1) it is an absolute method that does not require the use of standards, (2) this technique is quick with typical acquisition times of about 10 minutes, and (3) it is nondestructive. One of the disadvantages of RBS is that it has a poor sensitivity to light elements in heavy matrices. Some references which discuss Rutherford Backscattering Spectrometry (RBS) are Chu et al. 1978, Rimini 1995, Tesmer et al. 1995, and Schroder 1990.

Channeling RBS on a single crystal substrate allows for the determination of the lattice location of impurities, evaluation of crystalline quality, and the depth profile of lattice damage. For channeling RBS the sample is mounted on a goniometer. Figure 5.1 is a schematic diagram of the RBS setup for channeling experiments. The sample can be rotated through a tilt angle θ (rotation about the vertical axis) and azimuthal angle ϕ (rotation about the crystal normal).

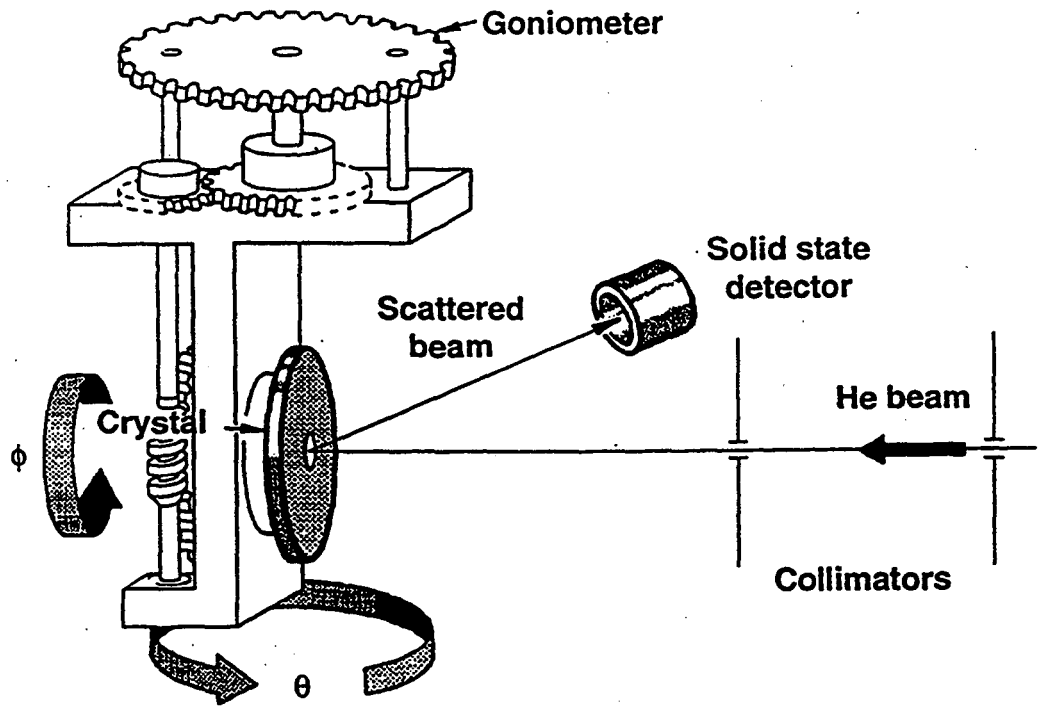

Figure 5.1 Schematic view of the setup for channeling experiments. The ion beam impinges on the sample mounted on a two axis goniometer (Tesmer et al. 1995).

A schematic diagram of the RBS process is illustrated in figure 5.2. The projectile ions are of mass M_1, atomic number Z_1, and energy E_0. M_2 and Z_2 are the mass and atomic number of the target (sample). Most of the incident ions lose their energies through electronic collisions and are stopped at some depth below the sample surface. A small fraction of these projectile ions undergo nuclear collisions with the target atoms and are backscattered. These ions lose energy traversing the sample, continue to travel towards the surface, and are detected by the detector. Using the principles of conservation of energy and momentum the kinematic relationship can be computed. The kinematic factor is defined as the ratio of the projectile's energy after the collision to its energy before the collision (E_1/E_0) and is given by:

$$k = \frac{\left[\sqrt{1-(R\sin\theta)^2} + R\cos\theta\right]^2}{(1+R)^2} \tag{8}$$

where R is defined by M_1/M_2 and θ is the scattering angle. In order to obtain high mass resolution the kinematic factor should be as large as possible. This can be achieved by placing the detector at a large angle with respect to the incident beam (close to 180°). The unknown mass of the sample can be calculated using the above kinematic expression, since E_1 can be measured and θ, E_0 and M_1 are known parameters.

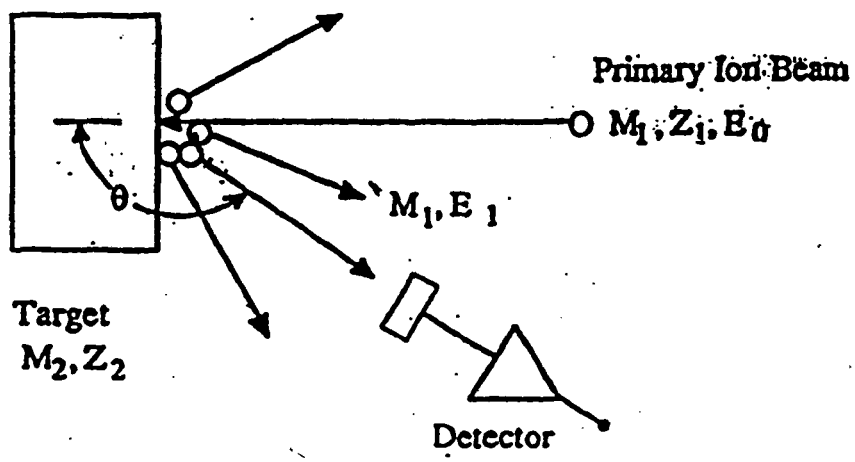

Figure 5.2 Schematic illustration of RBS setup.

The relative number of particles backscattered from a target atom into a given solid angle Ω for a given number of incident ions is related to the differential scattering cross section (Chu et al. 1978):

$$\frac{d\sigma}{d\Omega} = \left(\frac{Z_1 Z_2 q^2}{4E}\right)^2 \frac{4}{\sin^4\theta} \frac{\left[\sqrt{1-(R\sin\theta)^2} + \cos\theta\right]^2}{\sqrt{1-(R\sin\theta)^2}} \tag{9}$$

E is the energy of the projectile particle immediately before scattering. Typical values for scattering cross section of He particles are 1 to 10×10^{-24} cm^2/sr. Since $d\sigma/d\Omega$ can be accurately calculated quantitative measurement can be achieved by RBS. The scattering cross section is proportional to the square of Z_2 (target atomic number). As a result RBS is more sensitive to heavy elements than light elements. RBS allows one to determine the aerial density of atomic species at a depth x by measuring the height of the spectrum. The height of the spectrum (also called the backscattering yield) gives the total number of detected ions or counts. The backscattering yield can be calculated as follows:

$$A = \sigma \Omega Q N_s \tag{10}$$

Ω is the detector solid angle in steradians, Q is the total number of ions incidents on the sample, and N_s is the aerial density.

In addition to elemental and quantitative information, RBS is also depth sensitive. A particle which is backscattered from the bulk will have less energy than a projectile ion backscattered from the same element from the surface (see figure 5.3). This is because a particle below the surface has to undergo electronic collisions and loses energy in order to

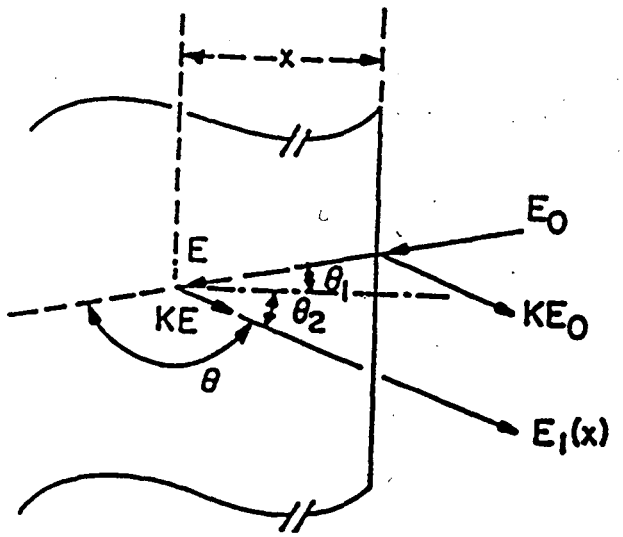

Figure 5.3 Schematic diagram of sample relative to the incident beam. The incident energy of the beam is E_o. The particles backscattered from a depth x from the surface exit the sample with $E_1(x)$.

traverse a distance x from the target surface. The projectile particle at a depth x below the sample surface loses energy on its way in (ΔE_{in}) and on its way out after it is backscattered (ΔE_{out}). Using these energy loss processes RBS can be used to determine the thickness of layers. The detected energy of the projectile ions backscattered from target atoms at a depth x which reaches the detector is given by:

$$E_1(x) = \left[E_o - \left(\frac{dE}{dx}\right)_{in} \frac{x}{\cos\theta_1}\right]K - \left(\frac{dE}{dx}\right)_{out} \frac{x}{\cos\theta_2} \qquad (11)$$

$$= KE_o - \left[K\left(\frac{dE}{dx}\right)_{in} \frac{1}{\cos\theta_1} + \left(\frac{dE}{dx}\right)_{out} \frac{1}{\cos\theta_2}\right]x$$

It is a ratio of the measured backscattered energy to the incident energy of the analyzing ion. The film thickness can be calculated from the energy difference from the projectile ions backscattered from the surface and the interface ΔE:

$$\Delta E = KE_o - E_1(x) = \left[K\left(\frac{dE}{dx}\right)_{in} \frac{1}{\cos\theta_1} + \left(\frac{dE}{dx}\right)_{out} \frac{1}{\cos\theta_2}\right]x = [S]x \qquad (12)$$

S is the backscattering energy loss factor. $S=N[\varepsilon]$ where N is the volume density and $[\varepsilon]$ is known as the backscattering stopping cross section factor. Values for the energy loss factor for He^+ ion in various materials are well known and can be found in many reference books (see for example Tesmer et al. 1995).

For solid phase epitaxial studies it is crucial to accurately measure amorphous layer thicknesses. To maximize ΔE for small change in x i.e., to improve depth resolution [S] should be maximized. The backscattering energy loss factor can be maximized by using the glancing exit angle geometry where θ_2 is large. In this geometry, the detector is placed

at a glancing exit angle (θ~100°with respect to the beam). A small change in depth measured along the normal corresponds to a large outgoing path and increased energy loss. The effect is to increase the ion path length required to reach a given depth in the sample measured perpendicular to the surface.

5.1.2 Ion Channeling

Channeling is a steering effect resulting from the Coulomb repulsion between the positive charged projectiles and the target atoms along rows or planes in a single crystal. Due to the steering action, the ions are directed towards the center of the channel. Since the ions do not come closer than the screening distance of the atoms the probability of large angle backscattering is reduced. A schematic illustration of the channeling phenomena is shown in the adjacent figure 5.4.

The critical angle for channeling is given by:

$$\Psi_c = \sqrt{\frac{2Z_1Z_2e^2}{Ed}} \quad \text{(radians)} \qquad (13)$$

Z_1 and Z_2 are the atomic numbers of the projectiles and target atoms, respectively. The spacing between the planes is given by d and e is the electronic charge (e^2=1.44x10^{-13}cm MeV). Ions entering near the center of a channel are steered within the channel if they are within the critical angle given in eq. 13. For MeV ^{4}He ions, the critical angle is usually 1 to 2 degrees. Channeling allows for the determination of the lattice location of impurities and the depth profile of the lattice damage if the analysis is performed on a single crystal substrate. Channeling RBS has been used extensively to study solid phase

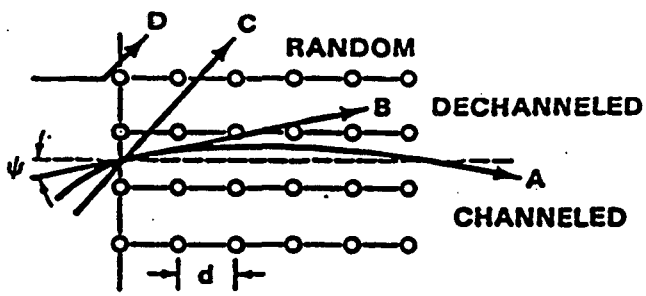

Figure 5.4 Illustration of channeling in a material.

epitaxial regrowth of ion implanted semiconductors. This technique has been reviewed in many references (Rimini 1995, Tesmer and Nastasi 1995).

Whether the thin film is amorphous or single crystal can be determined from channeling RBS. When a sample is channeled the rows of the atoms are aligned parallel to the incident projectile ions. Consequently, the projectile ions can penetrate deeply into the sample and have a low probability of becoming backscattered. When an ion beam is aligned with an axis of the single crystal substrate with an amorphous or polycrystalline overlayer, the channeled RBS spectrum shows the random yield (amorphous) for a certain energy width corresponding to the overlayer and then decreases. The decrease occurs at the crystalline/amorphous interface where channeling begins. The channeling yield from the substrate appears greater than that of a perfect single crystal because a larger fraction of the particles in the beam are dechanneled due to scattering when traversing the amorphous layer.

An ion beam aligned with a single crystal can be dechanneled by defects in the crystal. The ratio of dechanneling to channeling can be used to qualitatively gauge the extent of perfection of a crystal. The height of the spectrum (number of counts) in the underlying crystalline region depends on the thickness of the amorphous layer and decreases with amorphous layer thickness. In an amorphous layer, the aligned yield equals the random yield. Figure 5.5 shows the spectrum for a nearly perfect crystal, an amorphous layer, and a defective crystal. The surface peak for the aligned spectra corresponds to the scattering from the surface oxide layer.

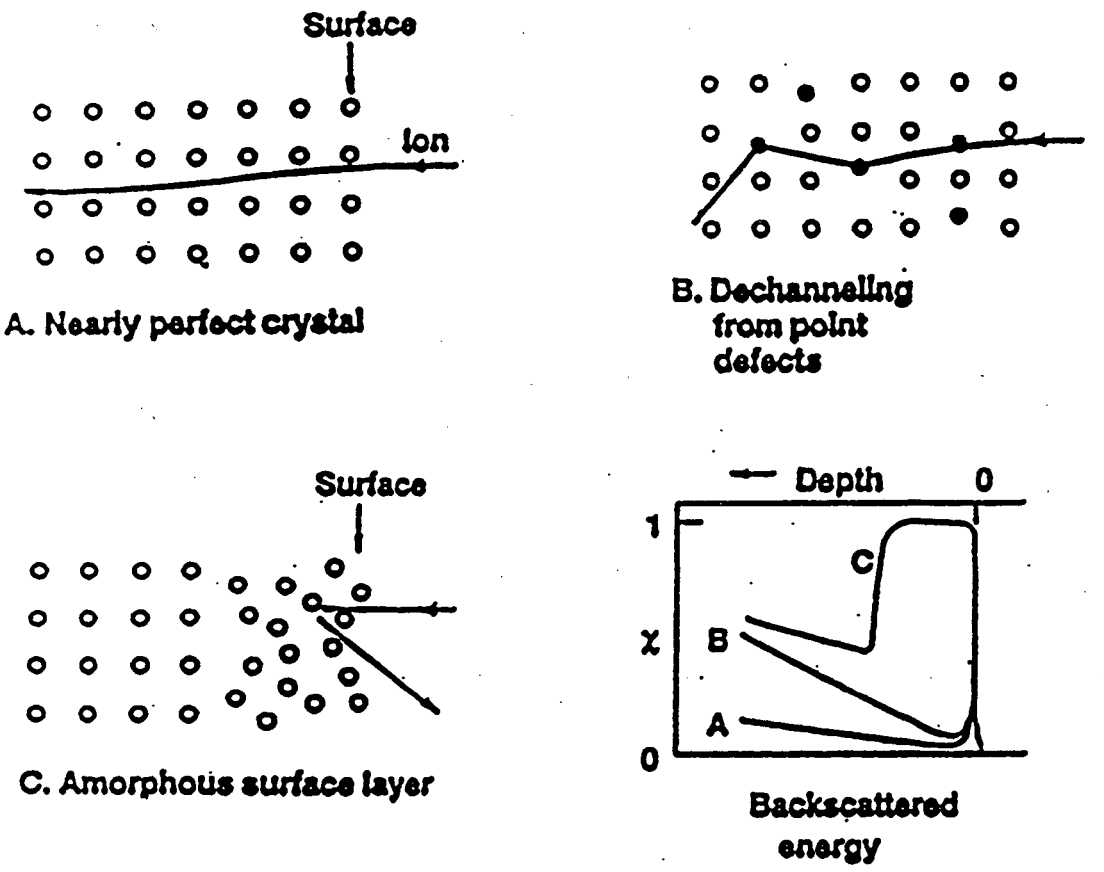

Figure 5.5 Channeling in (a) nearly perfect crystal, (b) crystal with point defects, (c) an amorphous material. The channeling RBS spectrum is for the three cases is shown in (d).

The normalized yield is:

$$\chi = \frac{\text{channeled yield } (\Psi = 0)}{\text{random yield } (\Psi > \Psi_c)} \tag{14}$$

χ is a measure for the fraction of dechanneled ions. The rate of change of χ with depth is proportional to the concentration of displaced host atoms. For an amorphous or polycrystalline material χ is one. In channeling RBS, an abrupt interface is indicated by a sharp step in the aligned spectrum.

5.2 Raman Spectroscopy

Raman scattering results from the interaction of incident light with optical phonons in a solid. There are two types of scattering which can occur, Stokes shifted scattering and anti-Stokes shifted scattering. In Stokes shifted scattering, the incident photon gives up part of its energy to the lattice in the form of an optical phonon. Hence, phonon emission takes place. In this type of scattering, the scattered photon emerges with a lower energy than the incident photon. The cross section for Stokes interaction is temperature independent. In anti-Stokes shifted scattering, the incident photon absorbs a phonon. Consequently, the incident photon emerges as a higher energy photon. Anti-Stokes intensities are strongly temperature dependent, since the number of phonons depends on the lattice temperature. For a one phonon process, conservation of energy and momentum yields:

$$\omega_s = \omega_i + \omega_q \tag{15}$$

$$k_s = k_i \pm q \tag{16}$$

where "s" is the scattered photon, "i" is incident photon, and "q" is the phonon. "k" and "q" are the photon and phonon wavevectors, respectively. "ω" is the frequency. Due to the fact that photon wavevectors are very small, only optical phonons at the center of the Brillouin zone are involved in Raman scattering. Depending on sample orientation, selection rules determine which lattice vibrations are observed (Swaminathan 1991). Table 5.1 shows the allowed modes for the various surface orientation for "ideal" semiconductors with the diamond or zinc blende structures.

Raman Spectroscopy is a characterization technique which is sensitive to crystal structure. It is a surface technique which can be used to probe the ion implanted layer. Some applications include information on the film crystallinity and the degree of disorder, the presence of amorphous layers, and the identification of symmetries of molecular structure and bonding.

In a defect free GaAs crystal the longitudinal optical (LO) phonon appears at 292 cm^{-1} (Desnica et al. 1992). Defects lead to broadening and shifting of the Raman lines as demonstrated in figure 5.6. In this study 100 keV Si ions were implanted in GaAs. As the dose was increased a shifting of the LO peak to lower frequencies was observed. At the highest dose, $3x10^{15}/cm^2$, broad bands characteristic for amorphous material were observed.

In another study (Braunstein 1989) where 1 MeV Si ions were implanted in GaAs at different doses (see figure 5.7), in addition to the LO peak, a transverse optical (TO) phonon was observed at 268 cm^{-1}. The TO phonon is forbidden for the (100) backscattering geometry. The authors suggested that the presence of this TO phonon is

Raman Active Mode	Surface Orientation		
	<100>	<110>	<111>
LO	Allowed[a)]	Forbidden	Allowed[a)]
TO	Forbidden	Allowed[a)]	Allowed[a)]

Table 5.1 Allowed modes for Raman scattering in "ideal" semiconductors for <100> <110>, and <111> surface orientations.

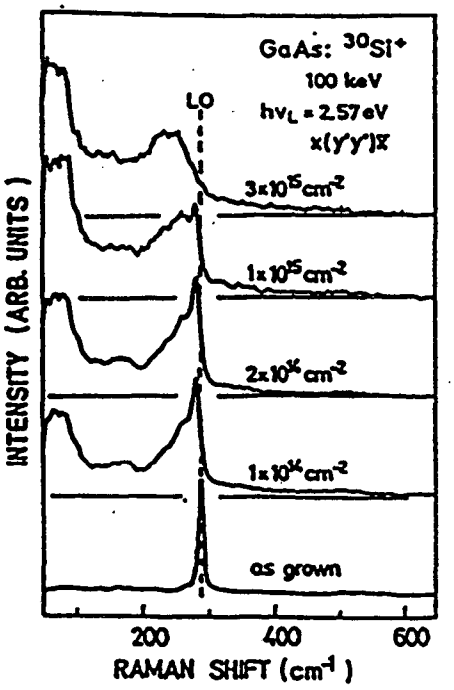

Figure 5.6 Raman spectrum for 100keV Si implanted in GaAs for various doses (Desnica et al. 1992).

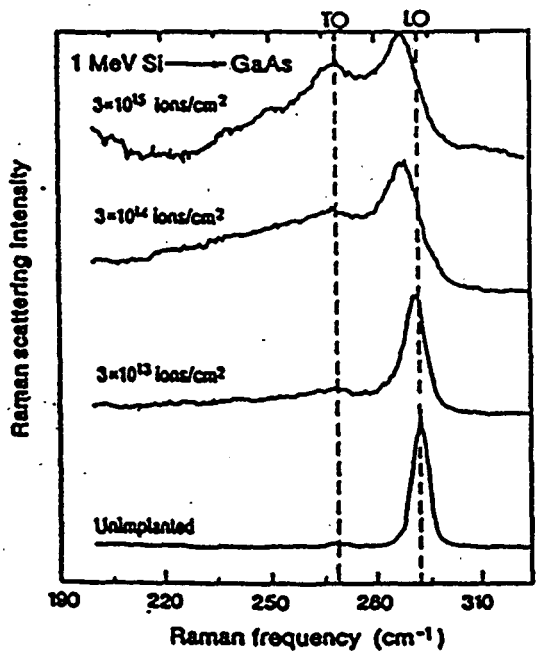

Figure 5.7 Raman spectra for 1 MeV Si implanted in GaAs for various doses (Braunstein 1989).

due to the pseudobackscattering geometry used and/or residual disorder. Our experimental observations support both propositions. We observe this peak in the unimplanted sample indicating that it would be attributed to the geometry. But, the intensity of the peak increases in the ion implanted and annealed layers, confirming that it is enhanced by the disorder in the crystal. The presence of the TO peak related to damage has also been suggested by Schroder (Schroder 1990).

5.3 Transmission Electron Microscopy

In Transmission Electron Microscopy (TEM) a parallel beam of electrons illuminates the specimen. It is essential that the sample be thin enough to transmit electrons. The transmitted and forward scattered electrons form a diffraction pattern in the back focal plane and an image is formed in the image plane. In the image mode, the diffraction lens is focused on to the image plane. Lenses are used to magnify the image. For the diffraction mode, the diffraction lens is focused onto the diffraction plane.

There are two methods for imaging in the TEM, conventional imaging and high resolution imaging. In the conventional imaging mode, the objective aperture (located in the back focal plane) is used to select one electron beam for imaging. For high resolution imaging many diffracted beams are allowed to contribute to the image.

TEM has been extensively used to examine the crystal structure and the microstructure of materials. It has extremely high resolution of the order of angstroms. The high resolution achieved in the electron microscope is attributed to the extremely small wavelengths of the electron beam. High Resolution Transmission Electron Microscopy (HRTEM), also called lattice imaging, yields structural information at the atomic level. It is widely used for interface analysis. Further information on TEM and HRTEM can be found in the references (Brundle et al. 1992; Schroder 1990, Loretto 1994). In this work, cross-sectional transmission electron microscopy was used to determine the position of the crystalline/amorphous interface and to obtain a detailed structure of the interfacial region.

6. Experimental Conditions

6.1 Sample Preparation

6.1.1 Implant Conditions

The Ion Beam Profile Code was used to calculate the implant ranges and determine the doses and energies for the implants. Multiple implants at different energies were used to obtain a uniform profile and suppress recrystallization from the surface (see figure 6.1). If the amorphous layer does not extend all the way to the surface, the regrowth can take place from both the surface and the bulk. As a result, a buried disordered layer can be formed.

Substrates used for the experiment were commercial semi-insulating (100)GaAs crystals grown by the liquid encapsulated Czochralski technique. The samples were solvent cleaned prior to implantation. Some of the samples were epi-ready and no solvent cleaning needed to be performed. Any extra cleaning would introduce contaminants. The samples which were solvent cleaned were boiled in trichloroethane, acetone, and then methanol for a few minutes, rinsed in methanol, and dried in flowing nitrogen.

Ion implantation was done in a Varian Extrion model CF-3000 implanter. The samples were tilted 7° away from the normal to prevent channeling during implantation. Most of the samples were implanted at LN_2 temperatures. One set of samples was implanted at room temperature for a study of the effect of implant temperature on the regrowth of the layers. For high dose rate implantations, the large flux of incident ions can lead to an increase in the temperature of the substrate. To avoid this or to minimize

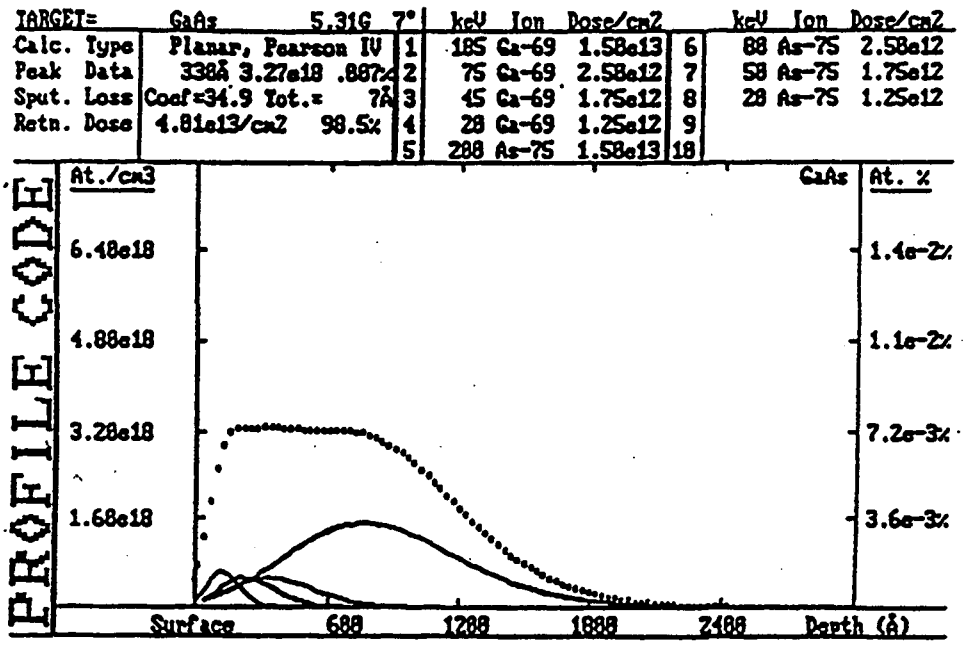

Figure 6.1 Ion Beam Profile simulation for multiple implants of Ga and As in GaAs.

this, it was important to have a good thermal contact between the substrate and the substrate holder. The implant conditions are shown in Appendix I.

6.1.2 Isochronal and Isothermal Annealing

Furnace annealing was performed in a horizontal tube furnace. For the high temperature anneals (greater than 500°C), the samples were sealed in a quartz ampoule. The ampoule was cleaned with 5% HF solution, rinsed with deionized water, methanol and then blown dry with N_2. The samples and pieces of solid As were cleaned in HCl and rinsed with deionized water. The quartz ampoule was evacuated. An atmosphere of As overpressure was used inside the ampoules. Sealing was done with a hydrogen torch. All samples were annealed in flowing N_2. For the high temperature anneals the sealed ampoules were annealed in flowing N_2.

6.2 Characterization

6.2.1 Rutherford Backscattering Spectrometry (RBS)

The RBS was performed at the Ion Beam Analytical Facility at the Lawrence Berkeley National Laboratory. The ion beam was generated by a 2.5 MeV Van de Graaff electrostatic accelerator. In these experiments a 1.8 MeV He^+ beam was used. Two silicon surface barrier detectors are installed in the chamber. One is located at 165° and the other at 100-120°. The samples are mounted on a two axis goniometer in the experimental chamber for channeling in the <100> or <111> directions. An electron suppression shield biased at -900V is used to suppress any secondary electrons. For each spectrum about 4μC of charge was collected at a beam current of about 10nA. To

minimize ion damage, after obtaining the channel by tilting and rotating the sample, the sample was translated to a fresh spot for data collection.

6.2.2 Raman Spectroscopy

The Raman spectra were obtained with a 488 nm Ar laser light. A pseudobackscattering geometry was used. The penetration depth of the laser light was approximately 60 nm. The data was collected without polarization discrimination for the scattered light. The laser was incident at 65° from the surface normal. The scattered light normal to the sample was collected by a camera lens and the image focused onto to the entrance slit of a single monochromater. All Raman spectra were collected at room temperature.

6.2.3 Transmission Electron Microscopy

Transmission Electron Microscopy (TEM) was performed one the samples using a JEOL 200CX high resolution electron microscope. Cross-sectional samples were prepared by mechanical grinding, followed by ion milling on a LN_2 cooled stage.

7. Results and Discussion

Good epitaxial recovery was achieved for stoichiometrically balanced ion implanted GaAs layers (i.e., amorphous GaAs layers created by implanting equal amounts of Ga and As ions in the same region). It was found that at low implantation doses, the co-implanted samples exhibited much better crystalline quality regrowth than the non-stoichiometrically balanced GaAs layers. First, SPE results of the "As-only", and "Ga-only" implanted samples will be discussed, proceeded by the co-implanted samples. In this manner, one is able to compare the role of stoichiometry in the low temperature SPE of the implanted GaAs layers.

The critical damage density required to make a layer amorphous is called the amorphization threshold. The low dose series was implanted at just above the amorphization threshold. From TRIM calculations and by measuring the as-implanted amorphous layer thicknesses, it is possible to calculate this amorphization threshold value. TRIM calculations were performed for all the doses and implanted energies used in this study. The displacement energies used in the calculations were 9.0 eV and 9.4 eV for Ga and As, respectively (Haynes and Stoneham 1985). The damage distribution was calculated for 18,900 ions. The distribution for the 185 keV Ga implanted GaAs to a total dose of $3x10^{13}$ions/cm^2 is shown in figure 7.0. The total damage density (left y-axis of plot) and the concentration of implanted ions (right y-axis of plot) are plotted. The total damage density was calculated by multiplying the vacancies produced by the ions and the recoils by the displacement energies of the host atoms. It can be observed from the calculations that the peak of the damage distribution is closer to the surface than the peak

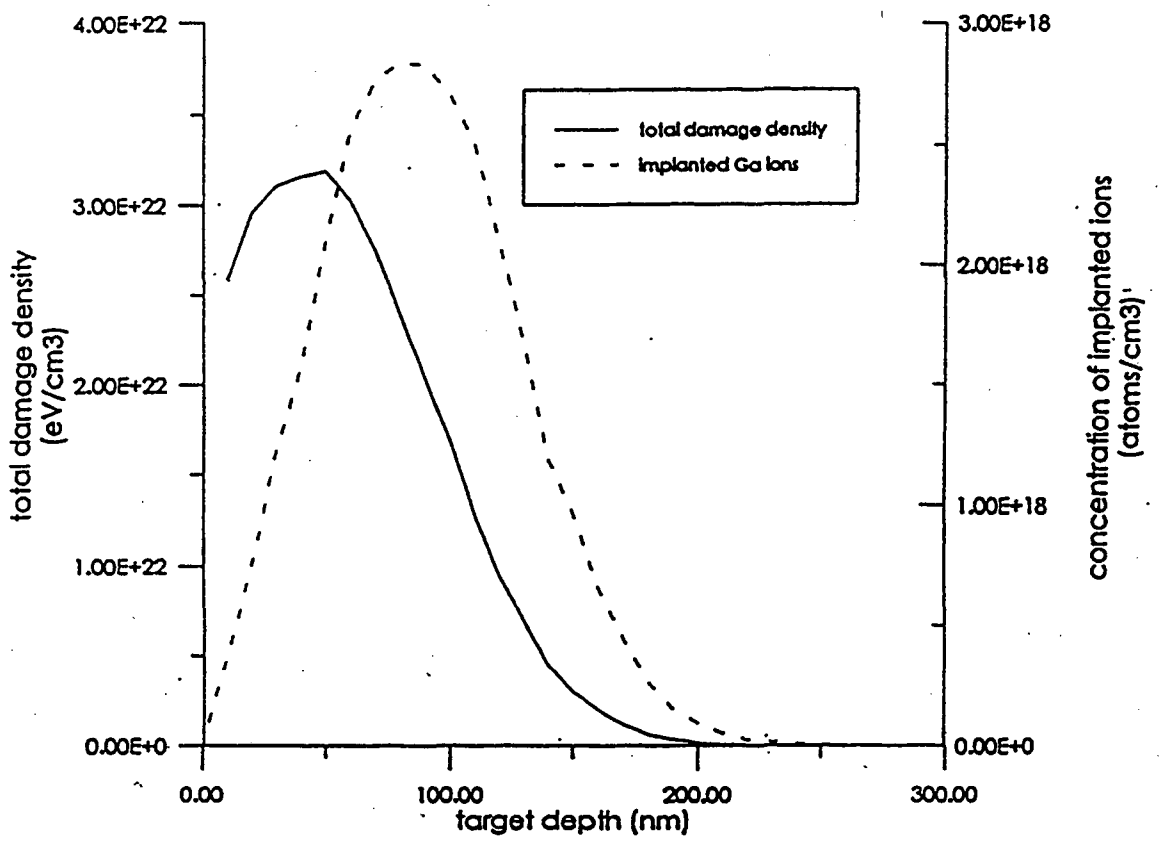

Figure 7.0 Trim calculations for 185 keV Ga ions implanted in GaAs with a total dose of $3x10^{13}/cm^2$. The total damage density distribution (left y-axis) and the concentration of implanted Ga ions (right y-axis) are shown.

of the concentration of implanted ions. This is due to the fact that near the end of the path of the ions, they no longer have sufficient energy to displace host atoms. As a result, the range of the damage does not match the distribution of the implanted ions. The amorphization threshold energy density for the co-implanted (A1-1), "As only" (A1-2) and "Ga only" (A1-3) were 3.2×10^{22} eV/cm^3, 2.8×10^{22}eV/cm^3, and 2.3×10^{22}eV/cm^3, respectively. It is evident from these results that a higher deposited energy density is required to amorphitize the co-implanted sample than the "As only" and "Ga only" samples. This is probably due to room temperature annealing of the co-implanted sample. These energy densities are in agreement with those published in the literature (Belay et al. 1995). These authors found that this critical energy density was independent of most implant parameters.

Cross-sectional TEM indicates that the as-implanted layer is not totally amorphous for all of the samples. The as-implanted layer is amorphous with regions of small crystallites. This partial amorphization can be attributed to the doses chosen near the amorphization threshold. Table 7.1 shows values for the amorphous layer for all three samples. The co-implanted sample exhibited the thinnest amorphous layer compared to the other samples. This thinner amorphous layer may be attributed to room temperature annealing which was only observed for the co-implanted sample.

The <100> aligned RBS spectra for the "As-only" implanted sample (A1-2) with a total dose of 3×10^{13}ions/cm^2 under various annealing conditions are shown in figure 7.1(a). The as-implanted was amorphous (i.e., the channel yield $\chi \sim 1$). For the lower temperature anneals (150°C and 200°C), the crystalline/amorphous interface proceeds

Sample	amorphous layer thickness (nm)	thickness of regrown layer with high stacking fault density (nm)
A1-1	52	27
A1-2	58	51
A1-3	58	31

Table 7.1 Values of thicknesses for the amorphous layer and the regrown layer (with high stacking fault density) for the "As only" (A1-2), "Ga only" (A1-3), and co-implanted (A1-1) samples.

(a)

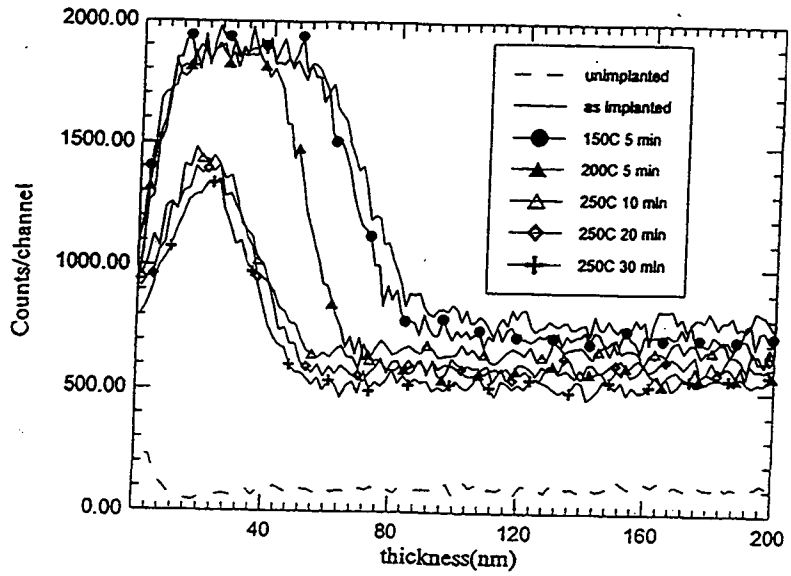

(b)

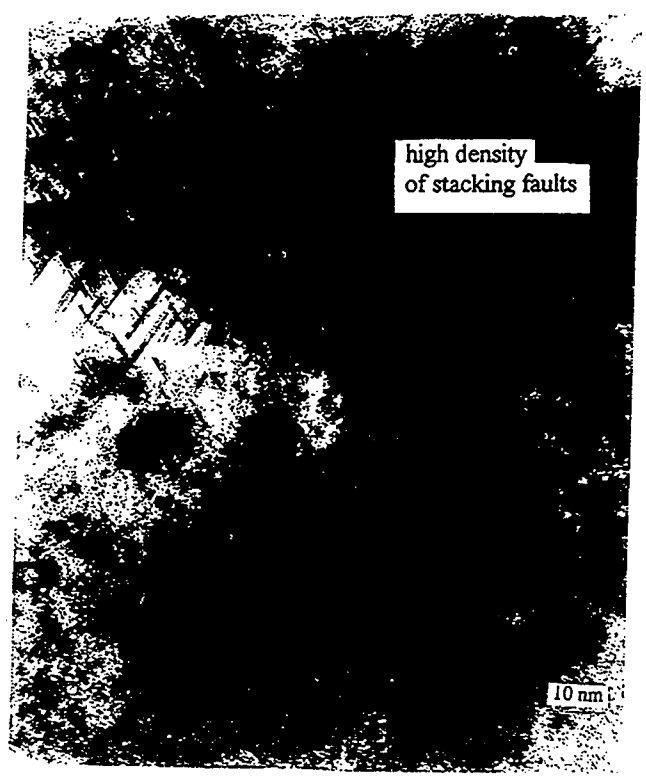

Figure 7.1(a) 1.8 MeV He^+ <100> aligned backscatter spectra for "As only" (A1-2) sample annealed at low temperatures. The samples were implanted with 200 keV As ions to a total dose of $3x10^{13}/cm^2$. (b) HRTEM micrograph of "As only" (A1-2) 250°C 30 min annealed sample.

towards the surface in a planar manner. This is revealed in the relatively sharp drop in the yield at the crystalline/amorphous interface indicating that the interface is sharp at these anneals. Significant regrowth occurs in the five min. anneal at 200°C. After the first 10 min. of the anneal at 250°C the regrown layer was crystalline with a highly defective region at about 30 nm below the surface. HRTEM was performed on the 250°C 30 min. annealed sample (figure 7.1(b)). A high density of stacking faults is observed ranging from the surface to about 48 nm into the bulk. End of range damage is observed as dark spots in the micrograph.

The as-implanted layer for the "Ga only" (A1-3) sample is also amorphous with small crystallites. This is confirmed by Raman spectra in which no amorphous broad band is observed. The regrowth behavior observed in the "Ga only" (A1-3) sample (figure 7.2(a)) is similar to the "As only" sample. SPE takes place at temperatures as low as 150°C. For the 10 min. anneal at 250°C about 40 nm of defect-free GaAs regrowth was observed . This is consistent with the observation that about 40 nm of an ion implanted GaAs layer can be regrown with zero residual disorder (Grimaldi et al. 1981). Additional annealing time appears not to improve the epitaxial quality of the layer. The TEM micrograph for the 250°C 30 min. annealed "Ga-only" (A1-3) sample is shown in figure 7.2(b). From the surface to about 20 nm the regrown layer contains defects. A high density of stacking faults are observed in the layer from 20 to 70 nm from the surface.

The RBS spectra for the co-implanted sample (A1-1) are displayed in figure 7.3(a). Similar to the "As-only" (A1-2) and "Ga-only" (A1-3) samples, SPE is initiated at temperatures of 150°C. It can be noted that in contrast to the "As only" and "Ga only"

(a)

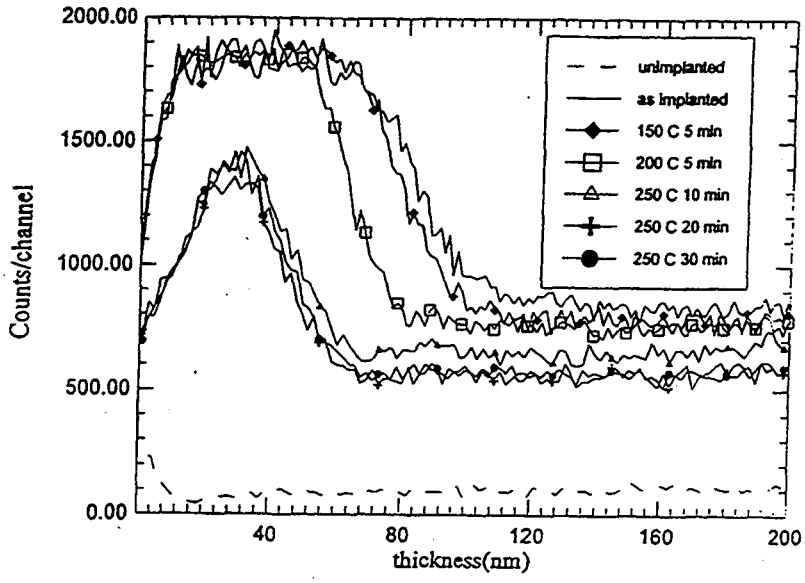

(b)

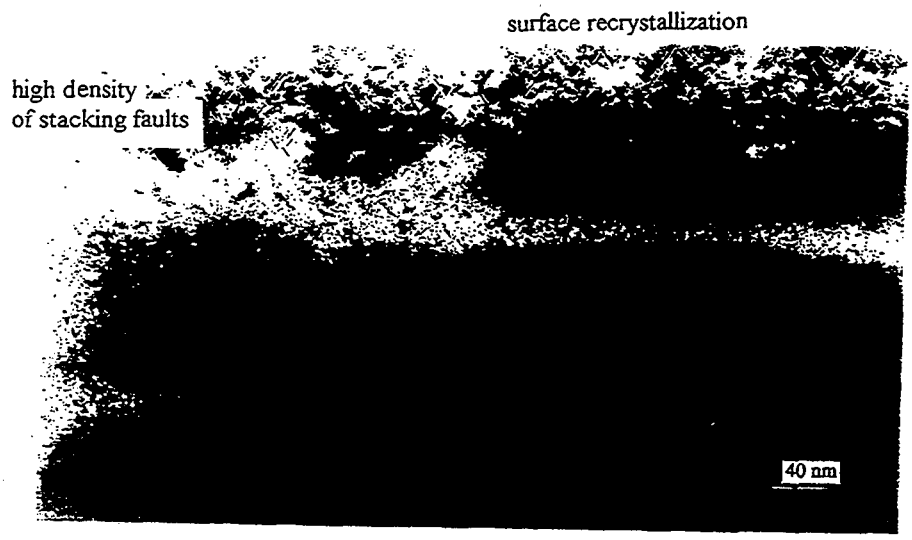

Figure 7.2(a) 1.8 MeV He^+ <100> aligned backscatter spectra for "Ga only" (A1-3) sample annealed at low temperatures. The samples were implanted with 185 keV Ga ions to a total dose of $3x10^{13}/cm^2$.(b) A cross-sectional TEM micrograph for the "Ga only" (A1-3) sample annealed at 250°C for 30 minutes.

(a)

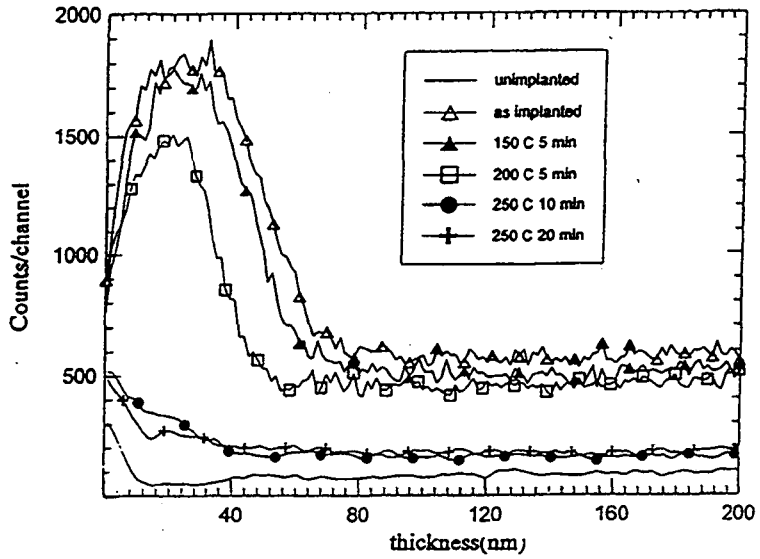

(b)

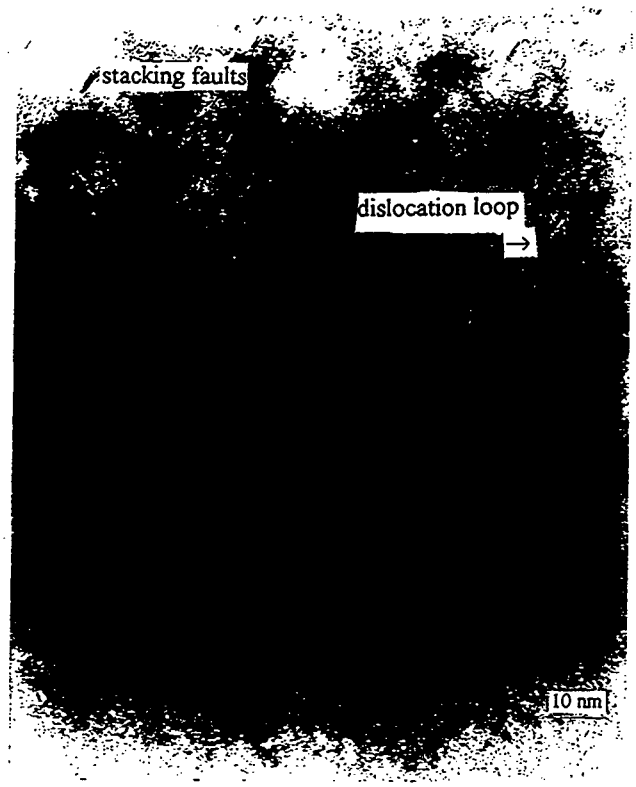

Figure 7.3(a) 1.8 MeV He^+ <100> aligned backscatter spectra for co-implanted sample (A1-1) annealed at low temperatures. The samples were implanted with 185 keV Ga ions to a total dose of $1.5x10^{13}/cm^2$, and 200 keV As ions to a total dose of $1.5x10^{13}/cm^2$. (b) HRTEM micrograph of co-implanted (A1-1) 250°C 30 min annealed sample.

samples after the 5 min. 200°C anneal the co-implanted sample is no longer amorphous. Significant regrowth occurs in the 5 min. anneal at 200°C as can be observed from the figure. The 250°C annealed samples showed good crystalline quality regrowth. It should be noted that most of the regrowth occurs in the first 10 min. of the annealing process. At this temperature, longer annealing times do not further improve the quality of the implanted layers. The HRTEM micrograph for the co-implanted (A1-1) sample annealed at 250°C for 30 min. is shown in figure 7.3(b). One of the most significant observations is that the stacking fault density in the co-implanted sample is much lower than in the "As-only" (A1-2), and "Ga-only" (A1-3) implanted samples. Figure 7.3(c) illustrates the Raman spectra for the co-implanted (A1-1) sample. The peak at 268 cm^{-1} is due to the transverse optical (TO) phonon. The TO mode is forbidden for the <100> zincblende structures. The TO peak observed in the unimplanted sample is most likely due to the pseudo-backscattering geometry used. The as-implanted sample exhibits the amorphous broad band which is in agreement with the TEM and RBS results. The LO peak in the annealed sample is slightly shifted compared to that of the unimplanted sample. This is an indication of the presence of defects. The ratio of intensities of the LO/TO peaks in the 20 min. annealed sample is about half to that of the unimplanted sample. This indicates that perfect epitaxially recovery has not been achieved.

It was necessary to determine if the improved crystalline quality achieved in the co-implanted sample was attributed to the warming up to room temperature in between the implantation of the two species. For this reason, another set of co-implanted samples was prepared which was maintained at LN_2 temperature for the entire implantation process

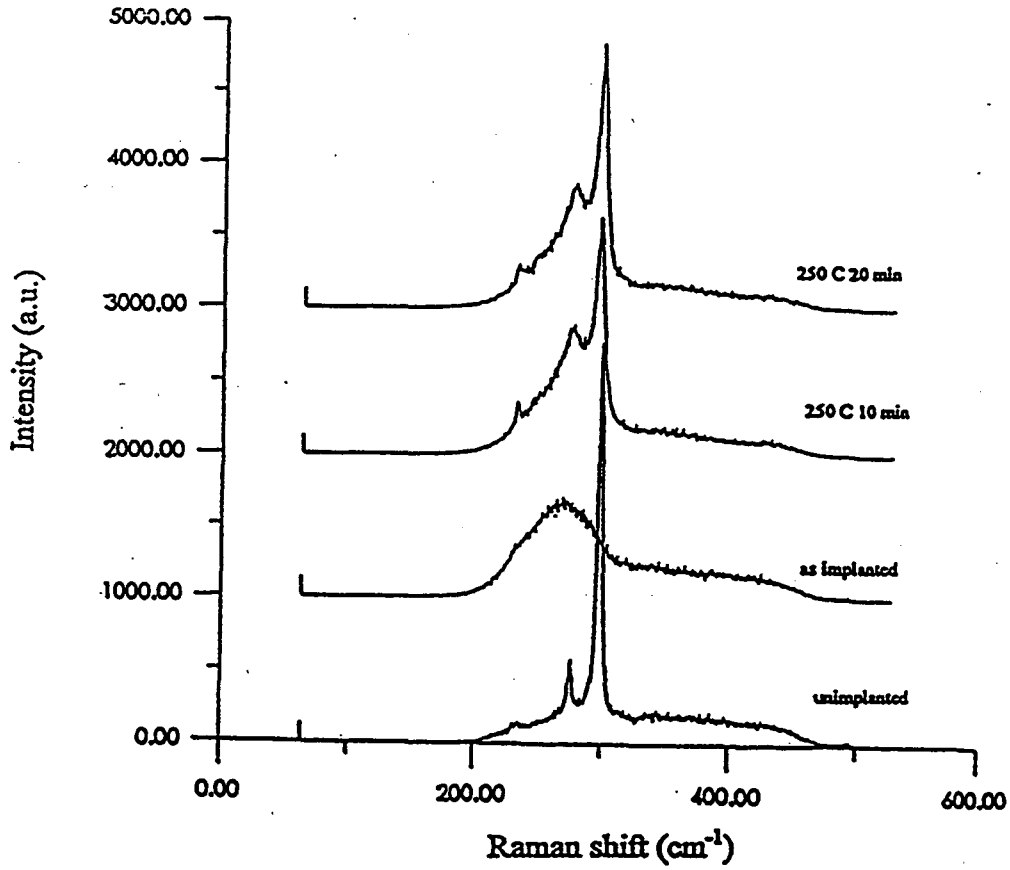

Figure 7.3(c) Raman spectra of co-implanted (A1-1) samples annealed at 250°C for 10 and 20 minutes. The samples were implanted with 185 keV Ga ions to a total dose of $1.5 \times 10^{13}/cm^2$, and 200 keV As ions to a total dose of $1.5 \times 10^{13}/cm^2$. The spectra were obtained by a multichannel spectrometer with 10mW laser power and 200-s integration.

(A1-1a). The amorphous layer was about 55 nm. This result confirms the finding that the co-implanted sample exhibits a thinner as-implanted amorphous layer than the "As only" and "Ga only" samples. In addition it eliminates the possibility that the thinner layer, as compared to the "Ga only" and the "As only", was due to the room temperature warming effects during the implantation process. The RBS spectrum for the A1-1a sample is presented in figure 7.4. It must be noted that this substrate was different from the other ones in the A series. It was miscut by a few degrees and as a result it was very difficult to channel the He^+ beam. The important features of the spectrum can still be extracted, however. It is evident that the co-implanted sample regrew significantly during the 250°C anneal. Again as in the case of the A1-1 sample, most of the regrowth occurred in the first 10 min. of the anneal. Good epitaxial recovery was achieved for this sample as indicated by the RBS backscatter spectrum. Analogous to the A1-1 sample perfect crystalline quality material was not obtained. Summarizing, both co-implanted samples (A1-1 and A1-1a) exhibited improved low temperature SPE regrowth as compared to the non-stoichiometrically balanced implanted layers.

In order to isolate the stoichiometric effects on the SPE regrowth of the implanted GaAs layers it is essential to take into account conditions which affect the regrowth, such as the previously discussed room temperature warming during implantation. Another issue of fundamental concern is the thickness of the as-implanted amorphous layers. A correlation between thickness of the amorphous layer and the residual defects remaining after annealing has been suggested (Grimaldi et al. 1981). These authors observed that a thinner amorphous layer regrows with less residual disorder. They extrapolated their

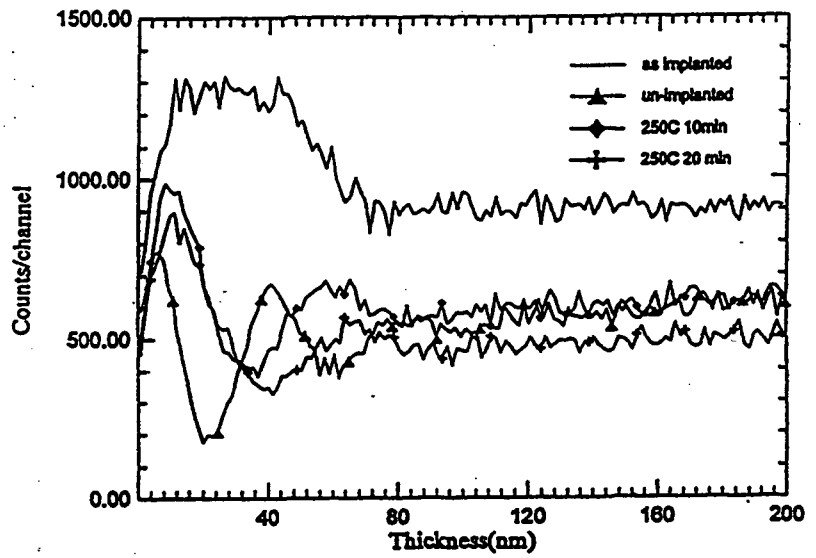

Figure 7.4 1.8 MeV He^+ <100> aligned backscatter spectra for co-implanted sample (A1-1a) annealed at low temperatures. The samples were implanted with 185 keV Ga ions to a total dose of $1.5x10^{13}/cm^2$, and 200 keV As ions to a total dose of $1.5x10^{13}/cm^2$.

results and concluded that a 40 nm ion implanted layer can regrow "perfectly." More recently reported values for this critical amorphous layer thickness are 30 nm (Belay et al. 1995) and 60 nm (Hurle 1994). It has been observed that in the initial stage of SPE in III-V materials, high quality single crystalline material can regrow about 60 nm from the original crystalline/amorphous interface (Hurle 1994). In the subsequent stages, growth is dominated by the formation of defects and dislocations, twinning, and by the nucleation of randomly oriented crystallites in the implanted layer near the crystalline/amorphous interface. Table 7.1 shows the thickness of the amorphous layer as measured from TEM micrographs for the "As only", "Ga only", and co-implanted samples. In addition, the thickness of the regrown layer which exhibited a high stacking fault density is shown in the table. From these results, it is apparent that about 25 nm of "twin free" recrystallized material was observed only for the "Ga only" and co-implanted samples. It appears that the excess As in the "As only" sample was accommodated by stacking faults resulting in the high density of these defects observed from the TEM micrograph.

Since the co-implanted layer had the thinnest amorphous layer, it can be argued that the improved regrowth observed in the co-implanted samples was due to the thinner as-implanted layer. To examine the effects of stoichiometry on the SPE regrowth of ion implanted GaAs, it was necessary to create thicker amorphous layers. The implantation conditions for the thicker amorphous layer samples ("B" and "C" series) are given in Appendix I. As noted in the table, the "B" and "C" series samples have the same implant conditions.

It was observed that for the high doses chosen, high quality single crystal material could not be obtained by the low temperature (250°C) SPE process for any of the samples. The spectrum for the "Ga-only" (B1-3) sample is illustrated in figure 7.5(a). The as-implanted amorphous layer thickness is about 132 nm. After annealing at 250°C for 10 min., regrowth occurred for approximately 10 nm. The regrowth is planar for the 10 and 20 min. anneal. After 30 min. the process is no longer dominated by a planar movement of the crystalline/amorphous interface. Therefore, longer annealing times (figure 7.5(b)) and higher temperatures were used to fully regrow the ion damaged layers. The samples were annealed at 250°C and 300°C for 4 hours and 20 min. each. The RBS spectra show that the annealed samples still exhibited a large amount of residual disorder. Since, the channeled yield $\chi \neq 1$ the annealed layer is no longer amorphous. It is highly defective single crystalline material. These temperatures were insufficient to repair the crystal damage. Samples were then annealed at higher temperatures (figure 7.5(c)). At 500°C, the crystalline/amorphous interface is non-planar. This phenomenon is distinctly different from the SPE regrowth of <100> and <110> Si which exhibits a planar crystalline/amorphous interface proceeding toward the surface. The non-planar crystalline/amorphous interface may be due local variations of stoichiometry at the interface. It has been reported that local non-stoichiometric regions within the amorphous layer in compound semiconductors can lead to breakdown of the crystalline/amorphous interface (Hurle et al. 1994). Finally at 700°C the residual disorder is removed.

Since As is volatile in the high temperature range (greater than 500°C) it was essential to determine if the annealing conditions result in degradation of the surface.

(a)

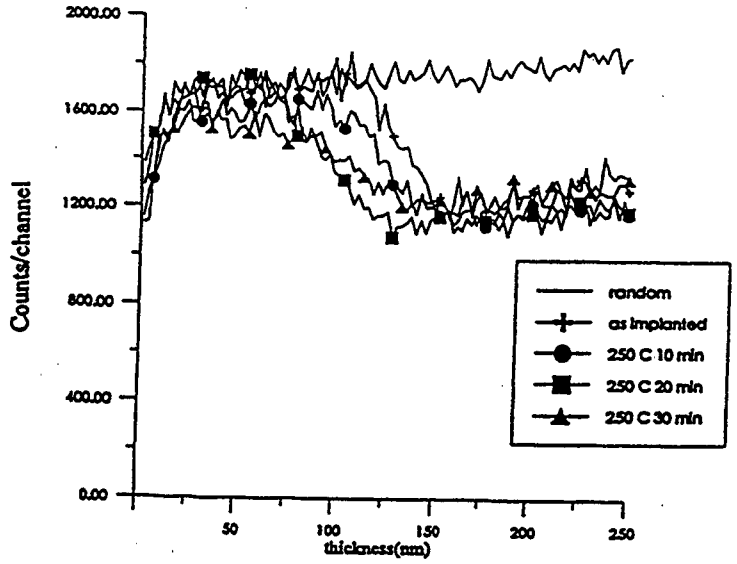

(b)

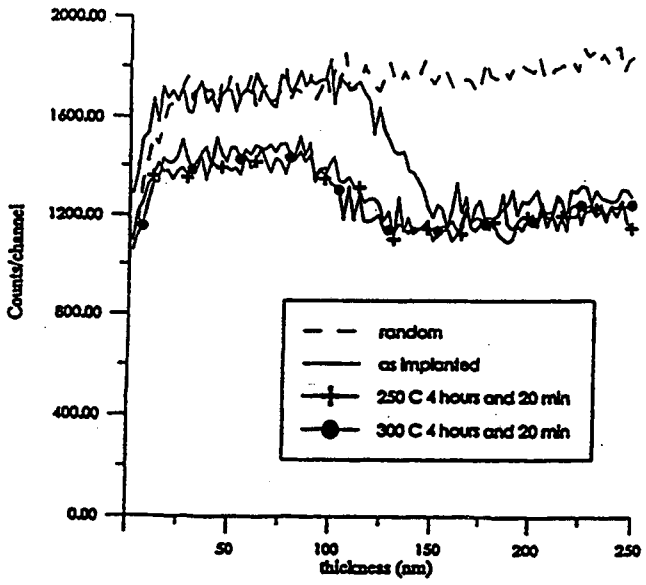

Figure 7.5 1.8 MeV He^+ <111> aligned backscatter spectra for (a) "Ga only" sample (B1-3) annealed at low temperatures. (b) "Ga only" sample (B1-3) annealed at 250°C and 300°C. The samples were implanted with 185 keV Ga ions to a total dose of $6.0 \times 10^{14}/cm^2$.

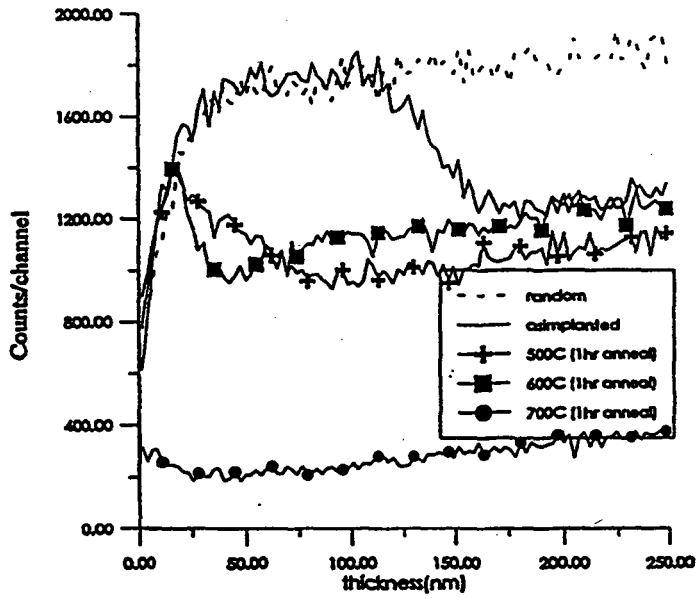

Figure 7.5 (c) 1.8 MeV He^+ <111> aligned backscatter spectra for "Ga only" sample (C1-3) annealed at high temperatures. The samples were implanted with 185 keV Ga ions to a total dose of $6.0 \times 10^{14}/cm^2$.

Raman spectroscopy was performed on the high temperature annealed samples. An unimplanted sample was annealed with the other samples (in the same ampoule) in order to examine the effect the high temperature annealing had on the substrate. Figure 7.6 shows the spectra for an unimplanted sample. The unimplanted sample annealed for 1 hour at 700°C exhibits good crystalline quality. The ratio of the transverse optical (TO) to longitudinal optical phonon (LO) is slightly higher in the annealed case. Nonetheless, it appears from this spectrum that the annealing conditions did not result in surface degradation.

RBS was performed on the high temperature annealed "As-only" (C1-2) samples (figure 7.7(a)). The samples were annealed at 500°C, 600°C, and 700°C for one hour each. Extensive regrowth occurred at the 500°C anneal as is evident from the spectrum, though a large amount of residual disorder is still present. For the 600°C annealed sample significant crystal defects are observed. For the 700°C annealed sample "perfect" epitaxial recovery was achieved. The Raman spectrum for this sample is presented in figure 7.7(b). The penetration depth of the laser is about 60 nm. Therefore, all of the signal should originate from the recrystallized layer. Valuable information can be extracted for comparison with the co-implanted sample which will be discussed later. The ratio of intensities of TO to LO peaks which is often used as a qualitative indication of the disorder in the crystal is greater in the annealed case than in the unimplanted sample. Consequently, it appears as if there is small amount of residual disorder. In order to confirm the high single crystal quality achieved in the 700°C annealed sample, electron microscopy still needs to be performed on this sample.

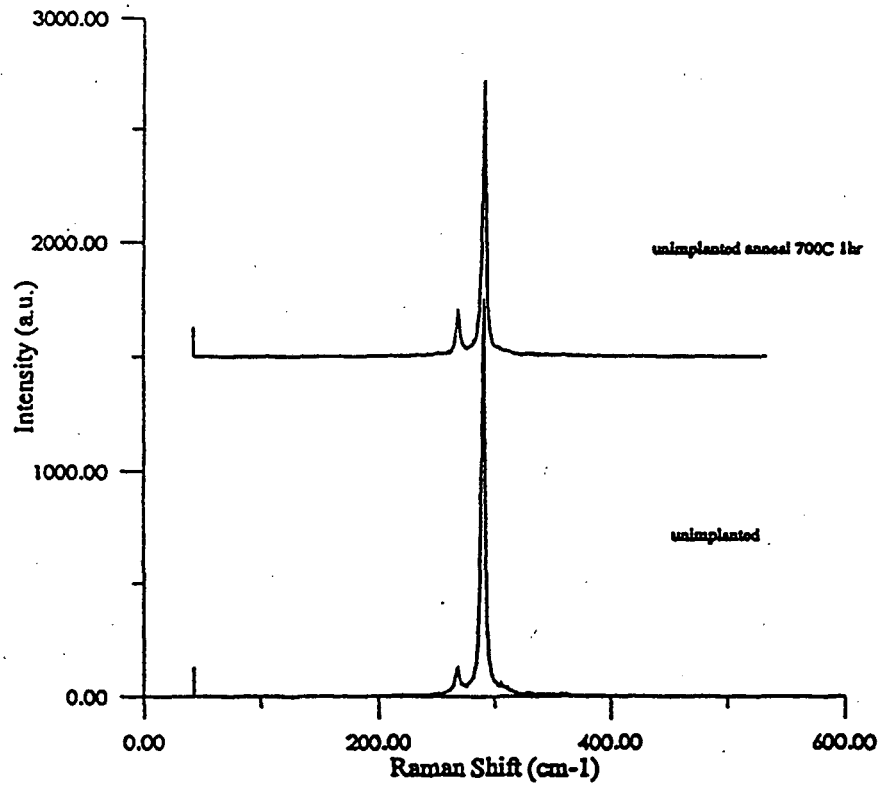

Figure 7.6 Raman spectra of "C" series substrates. The unimplanted substrate was annealed for 1 hour at 700°C.

(a)

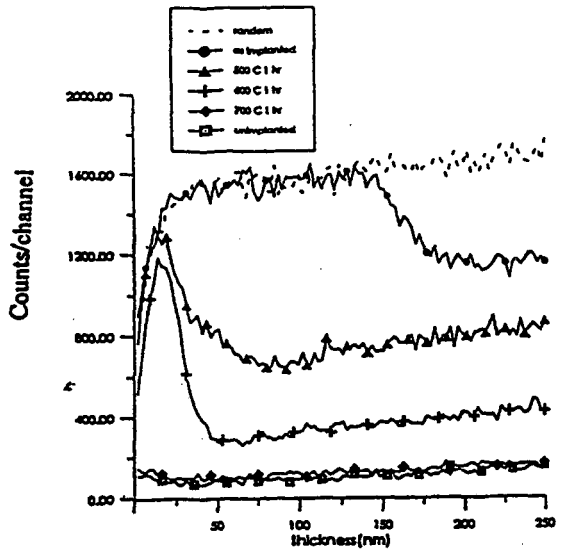

(b)

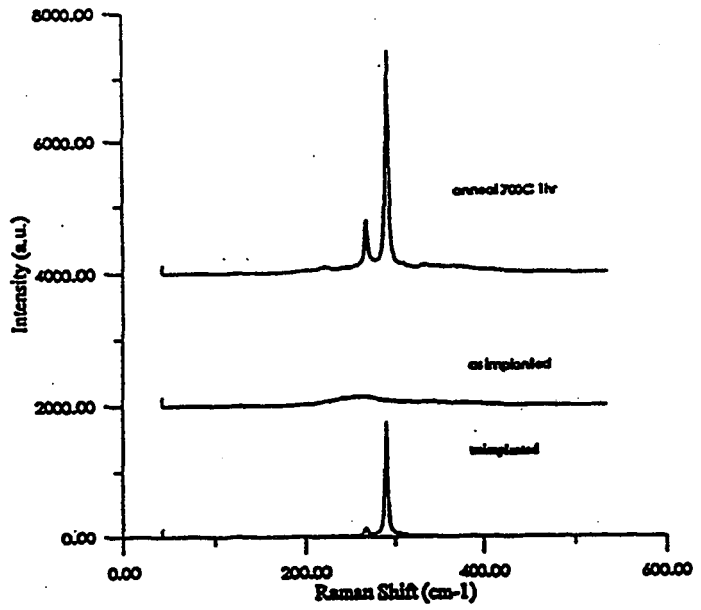

Figure 7.7 (a) 1.8 MeV He^+ <111> aligned backscatter spectra "As only" sample (C1-2) annealed at high temperatures. (b) Raman spectra of "As only" samples (C1-2). The samples were implanted with 185 keV As ions to a total dose of $5.6 \times 10^{14}/cm^2$.

The improved SPE regrowth behavior observed in the low dose stoichio-metrically balanced samples at low temperatures (250°C) was not found for the high doses. Analogous to the "Ga only" and "As only" implanted samples high temperature annealing (>500°C) was required to remove the residual disorder in the co-implanted samples. Two co-implanted samples were implanted with the same doses and energies. One sample was kept at LN_2 temperature for the entire implant process (B1-1) and the other was allowed to warm up to room temperature in between implant species (B1-1a). The as-implanted thickness of the B1-1a sample was about 10 nm less than the B1-1. This would be expected since some room temperature annealing occurred in the B1-1a sample.

A HRTEM micrograph for the B1-1 as-implanted sample is presented in figure 7.8. The implanted region is completely amorphous, no regions of crystallites are present as in the case of the low dose samples. The RBS spectra (figure 7.9(a)) shows that the regrowth proceeded in a planar SPE manner for the first 10 min.. This observation is evident upon comparing the slope at the crystalline to amorphous interface step in the spectra for the as-implanted and annealed sample. In perfect planar SPE an RBS spectrum will show a crystalline/amorphous interface which proceeds to the surface with a constant slope. After 20 min. of annealing roughening of the crystalline/amorphous interface is observed. In the 250°C 30 min. annealed sample at the crystalline/amorphous interface, microtwins along the {111} were observed (figure 7.9(b)) in addition to stacking faults in the recrystallized regions.

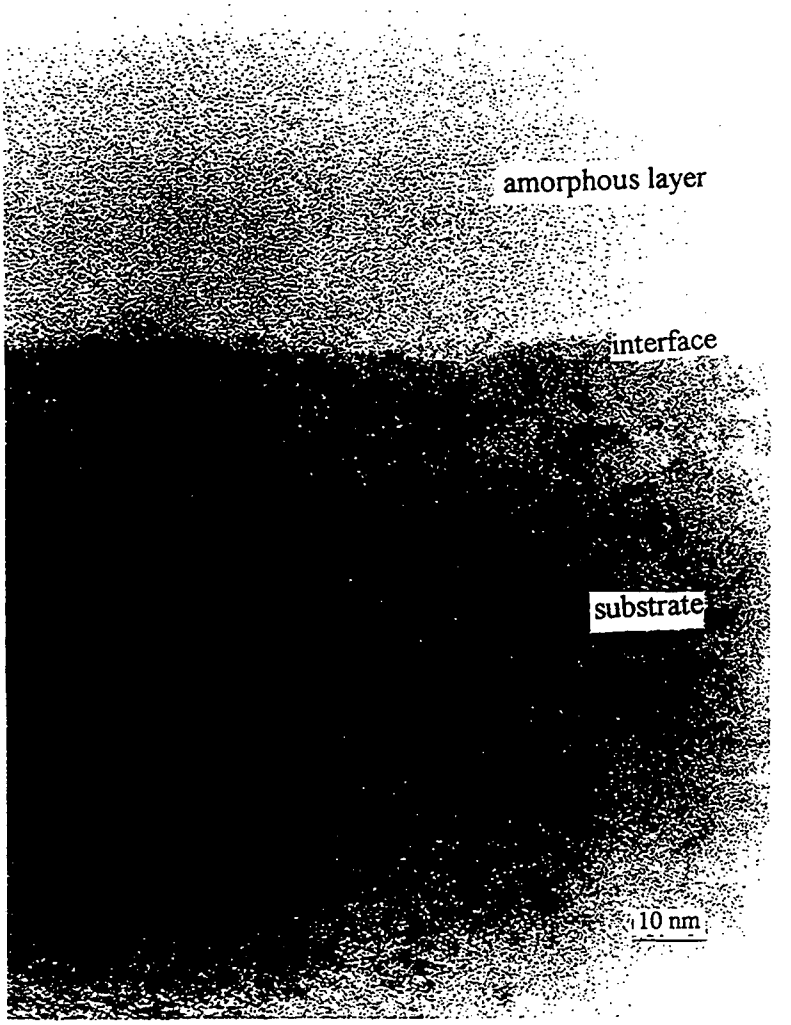

Figure 7.8 HRTEM micrograph of co-implanted (B1-1) as-implanted sample. The samples were implanted with 185 keV As ions and 185 keV Ga ions to a total dose of $3.0 \times 10^{14}/cm^2$ and $3.10 \times 10^{14}/cm^2$, respectively.

(a)

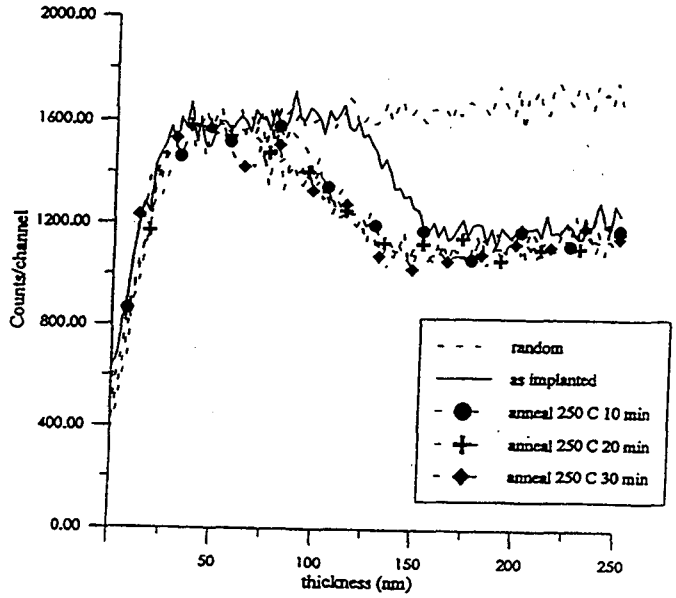

(b)

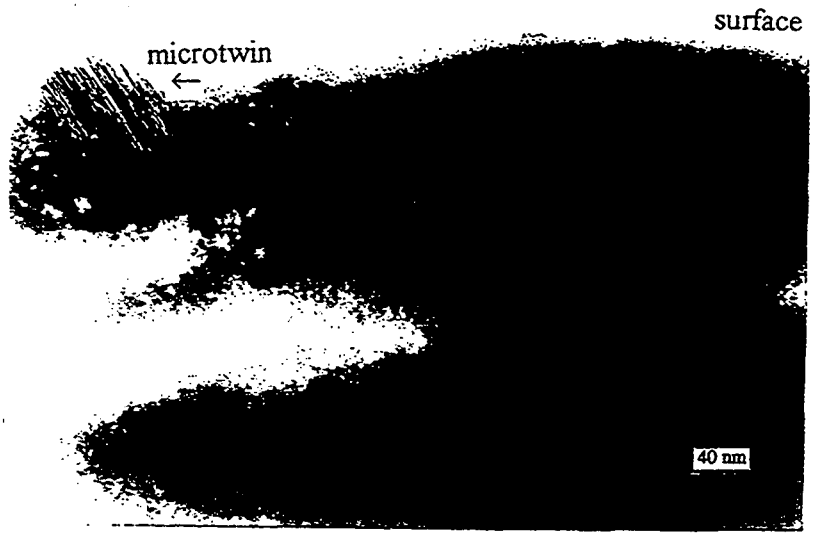

Figure 7.9 (a) 1.8 MeV He^+ <111> aligned backscatter spectra of co-implanted (B1-1) sample annealed at low temperatures. The samples were implanted with 185 keV As ions and 185 keV Ga ions to a total dose of $3.0 \times 10^{14}/cm^2$ and $3.10 \times 10^{14}/cm^2$, respectively. (b) A cross-sectional TEM micrograph co-implanted (B1-1) sample annealed at 250°C for 30 minutes.

The same regrowth behavior for low temperatures was observed in the B1-1a sample as compared to the B1-1 sample. One of the differences between the two samples is observed in the samples annealed at 250°C. At this low temperature the B1-1 sample regrew about 10 nm further than the B1-1a sample. Samples were annealed for longer times (4 hours and 20 min.) and slightly higher temperatures (300°C) in order to determine if the damage could be repaired given enough time at these temperatures. The RBS measurements indicated that under these annealing conditions a large amount of crystal disorder still remained (figure 7.10(a)). The HRTEM micrograph of the 300°C annealed sample reveals a high density of microtwins extending up to the surface (figure 7.10(b)). In addition, stacking faults are observed from 90 to 120 nm below the surface.

As is evident from these high dose results, low temperature annealing (250°C) is insufficient to anneal the crystal damage in the co-implanted samples (in contrast to the low dose case). The co-implanted samples (C1-1) were annealed at higher temperatures (500°C, 600°C, and 700°C) for 1 hour each. A large amount of crystal recovery was achieved after the 500°C anneal (figure 7.11(a)). After the 700°C anneal only a small amount of residual defects remain. This result is confirmed by Raman spectroscopy which shows that the 700°C annealed sample has a higher TO to LO intensity ratio as compared to the unimplanted sample (figure 7.11(b)). As previously mentioned, the ratio of TO/LO intensities can serve as indication of the crystalline quality of the material. It is interesting to observe that the ratio of the intensities of TO to LO is lower in the "As only" (C1-2)

(a)

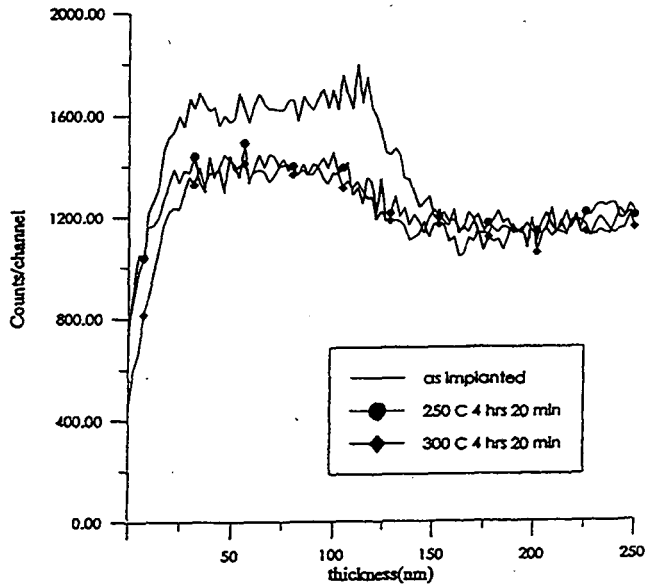

(b)

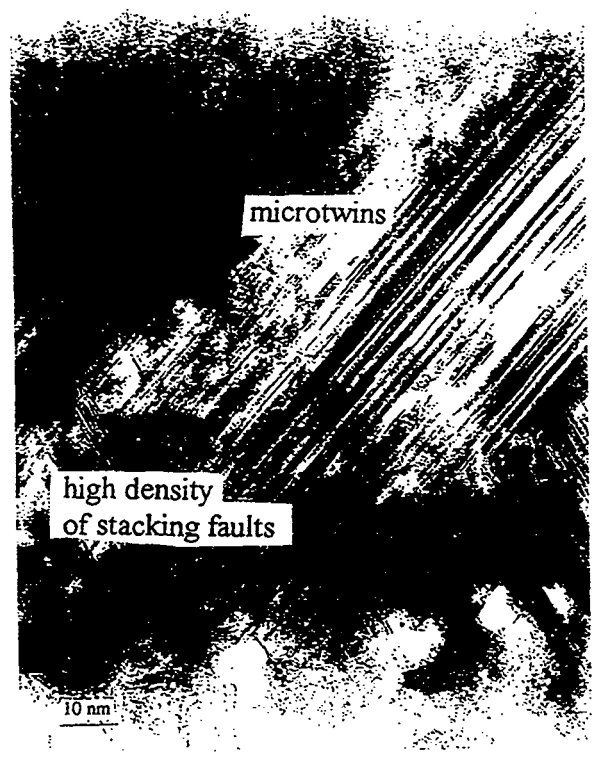

Figure 7.10 (a) 1.8 MeV He^+ <111> aligned backscatter spectra of co-implanted (B1-1) sample annealed at 250°C and 300°C for 4 hours and 20 minutes. (b) HRTEM micrograph of co-implanted (B1-1) sample annealed at 300°C for 4 hours and 20 minutes. The samples were implanted with 185 keV As ions and 185 keV Ga ions to a total dose of $3.0 \times 10^{14}/cm^2$ and $3.10 \times 10^{14}/cm^2$, respectively.

(a)

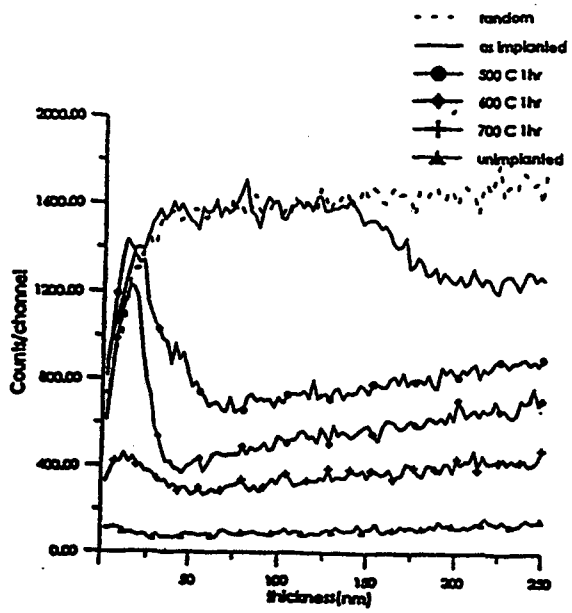

(b)

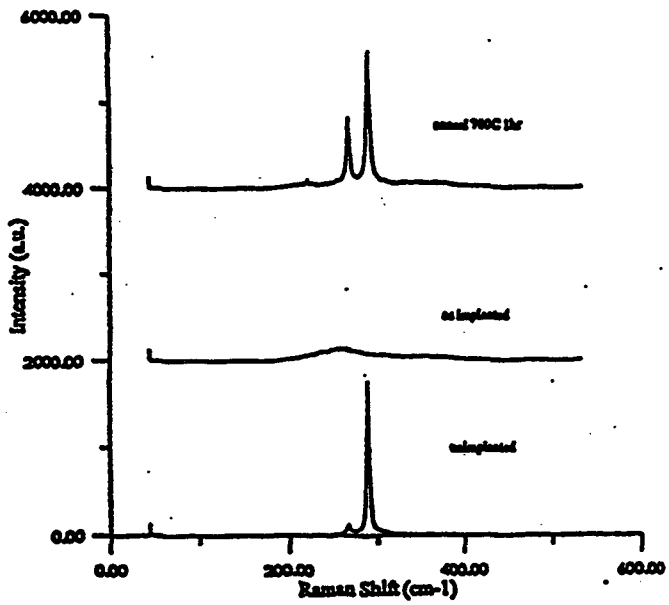

Figure 7.11 (a) 1.8 MeV He^+ <111> aligned backscatter spectra of co-implanted (C1-1) sample annealed at high temperatures. (b) Raman spectra of co-implanted (C1-1) sample of as implanted and 700°C annealed samples. The samples were implanted with 185 keV As ions and 185 keV Ga ions to a total dose of $3.0 \times 10^{14}/cm^2$ and $3.10 \times 10^{14}/cm^2$, respectively.

700°C annealed sample (figure 7.7(b)) than in the "co-implanted" sample (C1-1), suggesting that the "As only" annealed sample was of higher crystalline quality.

The high dose study revealed that improved epitaxial recovery was not achieved in the stoichiometrically balanced samples. These findings are in agreement with Belay et al. (Belay et al. 1995). These authors reported that even though macroscopic stoichiometry can be obtained by Ga and As co-implantation, due to the different recoils of the species microscopic non-stoichiometry is present in the amorphous layer. (The Ga mobility is also greater than As during annealing.) This microscopic non-stoichiometry increases with increasing total ion dose (Hurle 1994). This correlation is evident in the results obtained in this study.

Upon comparing the 700°C annealed "As only" and "Ga only" samples (figures 7.7(a)and 7.11(a)), it is apparent from the RBS spectra that the "As only" annealed sample exhibited less residual defects. It has been found that excess Ga has more detrimental effects on the SPE regrowth of amorphous GaAs than excess As (Belay et al. 1995).

8. Conclusions

This systematic study has shown that low temperature (250°C) SPE of stoichiometrically balanced ion implanted GaAs layers can yield good epitaxial recovery for doses near the amorphization threshold. For all of the samples annealed at 250°C most of the regrowth occurred in the first 10 min.. In order to accurately determine regrowth velocities and an activation energy for the process, further studies need to be performed at the lower annealing temperatures and at shorter annealing time intervals. HRTEM revealed a much lower stacking fault density present in the co-implanted sample than in the "As only" and "Ga only" samples with comparable doses. After low temperature annealing the non-stoichiometric samples exhibited a large amount of residual defects. The SPE regrowth of amorphous GaAs layers implanted with higher doses was also studied to determine if the enhanced epitaxial recovery observed in the co-implanted case could be attributed to the thinner amorphous layer. For these high doses very high temperatures (700°C) were needed to remove residual defects for all samples. The stoichiometrically balanced layer did not appear to regrow better than the "Ga only" and "As only" samples. This was explained by the effect of microscopic non-stoichiometry which is more pronounced at higher doses.

There are many issues which remain unresolved. For instance, it is unclear why the co-implanted sample exhibited a thinner amorphous layer than the "As only" and "Ga only" samples. It can be postulated that this may be attributed to room temperature annealing. The effects of room temperature annealing on the thickness of the as-implanted

amorphous layer were investigated for the low dose study. The as-implanted amorphous layer thickness was measured within the time period of a year. It was found that only the co-implanted sample exhibited room temperature annealing effects. The amorphous layer regrew about 5 nm. suggesting that stoichiometrically balanced amorphous layers can regrow even at room temperature. This factor would indeed account for the disparity in the observed amorphous layer thicknesses (see Table 7.1).

Another intriguing issue is the mechanism responsible for the solid phase crystallization in (100)GaAs. Two crystallization processes for amorphous layers which have been proposed are nucleation and growth of randomly oriented crystallites (RNG) and SPE. In pure amorphous Si, RNG becomes important only at extremely high temperatures. This is not observed for compound semiconductors. It has been reported that these two crystallization processes in compound semiconductors compete at much lower temperatures than in Si (Hurle 1994). For the low dose "As only" and "Ga only" samples annealed at low temperatures, it appears that both of these mechanisms are active. As mentioned previously for this amorphization threshold dose there remained crystallites in the amorphous layer for all of the as-implanted samples. Annealing at 250°C showed recrystallization from the surface (RNG) and the bulk (SPE) for these samples. For the co-implanted sample, the dominant mechanism involved is not as evident. More work needs to be performed in this area to elucidate the dominant recrystallization processes of amorphous GaAs layers.

9. References

P.A.Barnes, H.J.Leamy, J.M.Poate, S.D.Ferris, J.S.Williams, and G.K.Celler, Laser-Solid Interactions and Laser Processing, American Inst. Phys., NY 647 (1979)

C.R.Barrett, W.D.Nix, A.S.Tetelman, The Principles of Engineering Materials, Prentice-Hall Inc., NJ (1974)

R. Bauerlein, Radiation Damage in Solids, Academic Press, NY 358 (1962)

K.B.Belay, D.L.LLewellyn, and M.C.Ridgeway, Defect and Impurity Engineered Semiconductors and Devices, Materials Research Society PA (1995)

R.Bhattacharya, A.Rai, P.Pronko, J.Narayan, S.Ling, and S.Wilson, J.Phys. Chem. Solids **44**, 61 (1983)

J.S.Blakemore, Solid State Physics, Cambridge University Press, England (1985)

K.W.Böer, Survey of Semiconductor Physics, Van Nostrand Reinhold, NY (1992)

G.Braunstein, D.Tuschel, S.Chen, and S.-Tong Lee, J.Appl. Phys. **66** 3515 (1989)

C.R.Brundle, C.A.Evans Jr, S.Wilson, Encyclopedia of Materials Characterization, Butterworth-Heinemann, MA (1992)

Wei-Kan Chu, James W.Mayer, Marc-A Nicolet, Backscattering Spectrometry, Academic Press, NY (1978)

A.Claverie, A.Roumili, N.Gessinn, and J.Beauvillain, Materials Science and Engineering, **B4**, 205-209 (1989)

L.Csepregi, J.W.Mayer, and T.W.Sigmon, Phys. Lett. A **54**, 157 (1975)

L.Csepregi, E.F.Kennedy, T.J.Gallaher, and J.W.Mayer, J. Appl. Phys. **48**, 4234 (1977)

L.Csepregi, E.F.Kennedy, and J.W.Mayer, J.Appl. Phys., **49**, 3906 (1978)

B.L.Crowder, J.Electrochem. Soc. **117**, 671 (1970)

B.L.Crowder, J.Electrochem. Soc. **118**, 943 (1971)

U.V.Desnica, J.Wagner, T.E.Haynes and O.W.Holland, J.Appl. Phys **71**, 2591 (1992)

M.S.Dresselhaus, and R.Kalish, Ion Implantation in Diamond, Graphite and Related Materials, Springer-Verlag Berlin Heidelberg, NY (1992)

K.Gamo, T.Inada, J.W.Mayer, F.H.Eisen, and C.G.Rhodes, Rad. Effects **33**, 85 (1977)

M.G.Grimaldi, B.M.Paine, and M.A Nicolet, and D.K.Sadana, J. Appl. Phys. **52**, 4038 (1981)

M.G.Grimaldi, B.M.Paine, M.A.Nicolet, and D.K.Sadana, J.Appl. Phys. **53**, 1803 (1982)

C.R.M.Grovenor, Microelectronic Materials, Institute of Physics Publishing, PA (1989)

W.Haynes and A.M.Stoneham, Defects and Defect Processes In Nonmetallic Solids, John Wiley & Sons, NY (1985)

R.Heckingbottom, and T.Ambridge, Radiation Effects **17**, 31 (1973)

D.T.J.Hurle, Handbook of Crystal Growth: Thin Films and Epitaxy, North-Holland, Amsterdam (1994)

K.S.Jones, S.Prussin, and E.R.Weber, Appl. Phys. A **45**, 1 (1988)

K.S.Jones, and C.J.Santana, J.Materials. Res. **6:5**, 1048 (1991)

G.H.Kinchin and R.S.Pease, Rep. Prog. Phys. **18**, 1 (1955)

C.Kittel, Introduction to Solid State Physics, John Wiley and Sons, NY (1986)

J.Krynicki, H.Rzewuski, R.Groetzschel, and A.Claverie, Acta Physica Polonica A **79:2-3**, 349 (1991)

S.S.Kular, B.J.Sealy, K.G. Stephens, D.K.Sadana, and G.R. Booker, Solid State Electron. **23**, 831 (1980)

M.H.Loretto, Electron Beam Analysis of Materials, Chapman & Hall, NY (1994)

R.J.Malik, III-V Semiconductor Materials and Devices, North-Holland Elsevier Science Publishers B.V., Netherlands (1988)

J.W.Mayer, L.Eriksson, and J.A.Davies, Ion Implantation in Semiconductors, Academic Press, NY (1970)

J.W.Mayer, and S.S.Lau, Electronic Materials Science: For Integrated Circuits in Si and GaAs, Macmillan Publishing Company, NY (1990)

A.J.Moll, K.M.Yu, W.Walukiewicz, W.L.Hansen, and E.E.Haller, Appl. Phys. Lett. **60**, 2383 (1992)

A.J.Moll, J.W.Ager III, K.M.Yu, W.Walukiewicz, and E.E.Haller, J.Appl. Phys. **74**, 7118 (1993)

A.J.Moll, Ph.D. thesis, (1993a)

R.Morton, B.Zhu, S.S.Lau, and D.B.Poker, Appl. Phys. Lett. **66**, 1132 (1995)

F.G.Moore, H.B.Dietrich, and E.A.Dobisz, Appl. Phys. Lett. **57:9**, 911 (1990)

R.S.Muller, and T.I. Kamins, Device Electronics for Integrated Circuits, John Wiley & Sons Inc. NY (1986)

H.Narayanan, and A.Kachare, Phys. Status Solidi. **26**, 657 (1974)

G.L.Olson, and J.A. Roth, Materials Science Reports, **3**, 1 (1988)

S.J.Pearton, J.M.Poate, F.Sette, J.M.Gibson, and D.C.Jacobson, Nucl. Instr. and Meth. **B19/20**, 369 (1987)

J.Poate, and J.Williams, Ion Implantation and Beam Processing, Academic Press NY (1984)

E.Rimini, Ion Implantation: Basics to Device Fabrication, Kluwer Academic Publishers, MA (1995)

H.Ryssel and I.Ruge, Ion Implantation, John Wiley & Sons, NY (1986)

D.Schroder, Semiconductor Material and Device Characterization, John Wiley & Sons Inc, NY (1990)

B.J.Sealy, Int. Mat. Rev **33**, 38 (1988)

H.J.Stein, F.L.Vook, D.K.Brice, J.A.Borders and S.T.Picraux, Proceedings of The 1st Conference on Ion Implantation, Gordon and Breach, London (1972)

V.Swaminathan, and A.T.Macrander, Materials Aspects of GaAs and InP Based Structures, Prentice Hall, NJ (1991)

J.R.Tesmer, M.Nastasi, J.C.Barbour, C.J. Maggiore, J.W.Mayer, Handbook of Modern Ion Beam Materials Analysis, Materials Research Society, PA (1995)

K.N.Tu, J.W.Mayer, and L.C.Feldman, Electronic Thin Film Science For Electrical Engineers and Materials Scientists, Macmillan Publishing Company, NY (1992)

E.Wendler, W.Wesch, and G.Götz, Phys. Stat. Sol. A **112**, 289 (1989)

W.Wesch, E.Wendler, and G.Götz, J.Appl. Phys. **65:2**, 519 (1989)

J.S.Williams, and M.W.Austin, Appl. Phys. Lett. **36**, 994 (1980)

V.L.Wrick, W.J.Choryke and C.F.Tseng, Electron. Lett. **17**, 752 (1981)

J.Ziegler, J.P.Biersack, J.Cuomo, unpublished (1980)

J.Ziegler, J.P. Biersack, U.Littmark, The Stopping Range of Ions in Solids, Pergamon, New York (1985)

Appendix I Implant Conditions

Sample	Implant Ion	Energy (keV)	Dose(atoms/cm^2)
A1-1*	Ga	185	1.50×10^{13}
	Ga	75	2.50×10^{12}
	Ga	45	1.75×10^{12}
	Ga	20	1.25×10^{12}
	As	200	1.50×10^{13}
	As	80	2.50×10^{12}
	As	50	1.75×10^{12}
	As	20	1.25×10^{12}
A1-1a	Ga	185	1.50×10^{13}
	Ga	75	2.50×10^{12}
	Ga	45	1.75×10^{12}
	Ga	20	1.25×10^{12}
	As	200	1.50×10^{13}
	As	80	2.50×10^{12}
	As	50	1.75×10^{12}
	As	20	1.25×10^{12}
A1-2	As	200	3.00×10^{13}
	As	80	5.00×10^{12}
	As	50	3.50×10^{12}
	As	20	2.50×10^{12}

Appendix I Implant Conditions

Sample	Implant Ion	Energy (keV)	Dose(atoms/cm^2)
A1-3	Ga	185	3.00×10^{13}
	Ga	75	5.00×10^{12}
	Ga	45	3.50×10^{12}
	Ga	20	2.50×10^{12}
B1-1(C1-1)	Ga	185	3.10×10^{14}
	Ga	75	5.00×10^{13}
	Ga	45	2.60×10^{13}
	Ga	33	1.00×10^{13}
	As	185	3.00×10^{14}
	As	75	4.90×10^{13}
	As	45	2.50×10^{13}
	As	33	1.00×10^{13}
B1-1a*	Ga	185	3.10×10^{14}
	Ga	75	5.00×10^{13}
	Ga	45	2.60×10^{13}
	Ga	33	1.00×10^{13}
	As	185	3.00×10^{14}
	As	75	4.90×10^{13}
	As	45	2.50×10^{13}
	As	33	1.00×10^{13}

Appendix I Implant Conditions

Sample	Implant Ion	Energy (keV)	Dose(atoms/cm^2)
B1-2(C1-2)	As	185	5.60×10^{14}
	As	75	9.60×10^{13}
	As	45	4.80×10^{13}
	As	33	1.00×10^{13}
B1-3(C1-3)	Ga	185	6.00×10^{14}
	Ga	75	1.00×10^{14}
	Ga	45	5.20×10^{13}
	Ga	33	1.10×10^{13}

note: 1)all implants are at entirely at LN_2 temperatures except "*". This implant was done at LN_2 but the sample was warmed up in between implant species.
2)B and C series have the same implant conditions

LAWRENCE BERKELEY LABORATORY
CENTER FOR ADVANCED MATERIALS
1 CYCLOTRON ROAD
BERKELEY, CALIFORNIA 94720